UNIVERSITY OF COPENHAGEN
FACULTY OF SCIENCE

Master Thesis

Cecilie Toftdahl Olesen

Efficient Generation of Pure and Indistinguishable Single Photons

Peter Lodahl and Ravitej Uppu

Handed in: September 30, 2020

Master Thesis

Efficient Generation of Pure and Indistinguishable Single Photons

Author:	**Cecilie Toftdahl Olesen**
Supervisor:	Prof. Peter Lodahl
Supervisor:	Asst. prof. Ravitej Uppu

Submission Date: September 30, 2020

Quantum Photonics

Center for Hybrid Quantum Networks (Hy-Q)
The Niels Bohr Institute
University of Copenhagen

Abstract

High-quality single-photon sources are a vital part for realizing many quantum information protocols [1]. In this thesis quantum dots embedded in photonic crystal waveguides have been studied for the purpose of generating high indistinguishable single photons. High indistinguishability is achieved by optically exciting the exciton in a quantum dot using a pulsed laser with frequency on resonance with the exciton transition. However, resonant excitation introduces the challenge of suppressing laser scattering in the collected emission. This directly limits the purity of the source.

The waveguide creates a spatial separation between the excitation of the quantum dot and the collected emission. This allows for the purity to be high, as collection mainly consists of photons emitted from the quantum dot.

This begs the question of how pure a single photon emission can be generated on this type of platform. This has been studied by estimating purity, indistinguishability, and efficiency of the single-photon source. The main focus of this thesis has been on investigating how the wavefront and shape of the excitation pulse influences the quality of the source. This includes studying how the pulse duration of the excitation laser influences the purity. The pulse duration should be short enough to not cause multi-photon emission, while not so short that it introduces laser scattering. Instead of changing the shape of the pulse one may also alter the wavefront. One approach is to adjust the polarization of the wavefront. The efficiency of which the quantum dot is being excited is directly affected by the overlap between the polarization of the excitation laser and the orientation of the quantum dot dipole. Therefore, this should be optimized for. However, for some spin-photon interface and multi-photon protocols it might be a requirement to selectively excite a given polarized dipole, where scattering is not naturally suppressed. It is in this work reported how modifying the phase of the incident wavefront can improve the purity at a given polarization.

The best achieved single photon emission was measured to have a purity of $g^2(0) = 0.0086 \pm 0.0013$ and indistinguishability of $V = 96 \pm 1\%$ with a total efficiency of $6 \pm 1\%$, which results in a detected photon rate of 2.6 million photons per second, using a pulsed laser of 76 MHz repetition rate. Concurrently achieving such a high-quality across all three parameters shows how quantum dots embedded in photonic crystal waveguides are promising candidates as state-of-the-art single-photon sources.

Acknowledgements

First of all I wish to thank my supervisors Peter Lodahl and Ravitej Uppu for giving me the opportunity to work on my thesis in the Quantum Photonics group. Thank you to Peter for introducing me and igniting my interest in quantum optics. I would like to give a special thanks to Ravi for spending countless hours teaching me all that I know about quantum photons and working in a lab, as well as for his endless patience. A great thanks to Freja for helping me to learn everything from building mirrors to analyzing data and for many good discussions. To everyone in the Quantum Photonics group, I feel very fortunate for having shared my days in such an enriching space - Thank you for creating such a nice and informal work environment. To my friends studying physics with me for the support through not only this last year, but the entirety of my physics degree, and for the comfort of our friendship, for that I am very thankful. Lastly but not least, to my family for all the courage, love, and support. Thank you.

Contents

CHAPTER 1
Introduction

This chapter consists of a brief introduction to quantum light generation through light-matter interaction. It is meant to serve as the framework for the further chapters of this thesis.

Many quantum information protocols including quantum key distribution [2], quantum repeaters [3], and quantum simulators [4] require the realization of on-demand high-quality single-photon sources in order to generate non-classical photons to serve as carriers.

On-demand meaning a deterministic single-photon source where exactly one photon is being generated each time the system is being probed. While high-quality refers to light pulses of well-defined wavepackets with near-unity indistinguishability. Such a source is expected to rarely emit a wrong number of photons and to have high efficiency [1].

The focus of this thesis is to study the quality of single photons and understand what phenomenons limits the intrinsic purity.

1.1 Two-Level System

The state-of-the-art approach for generating single photons is in its core straightforward: a single quantum emitter is excited with a pulsed laser and the emission is then collected, see Figure 1.1.

The quantum emitter is in its simplest form described as a two-level system (TLS) [5]. It can be defined as being initially in a superposition between the ground state $|g\rangle$ and the excited state $|e\rangle$ with some probability P_e:

$$|\psi_i\rangle = \sqrt{(1-P_e)}\,|g\rangle + \sqrt{P_e}\,|e\rangle \tag{1.1}$$

With probability P_e a single photon is emitted at rate γ. This phenomenon is known as spontaneous emission and governs the dynamics of the system as the excited state decays to the ground state by emission of a single photon. This is what allows for the TLS to be employed as an ideal single-photon source. However, after decaying to the ground state the system is stable and nothing happens until it becomes excited again.

So in order to achieve an on-demand source the TLS is being driven by short laser pulses with frequency on resonance with the TLS transition. This is known as resonance fluorescence. The emission from the TLS will ideally be a Lorentzian single-photon wavepacket and the photons can be emitted in any direction. The system behaves as an ideal on-demand single-photon source if it responds with a single photon each time it is being probed.

A quantum dot (QD) can behave as a TLS under the right circumstances. Figure 1.2 is a sketch of the energy levels of a neutral exciton X^0, consisting of the ground state $|0\rangle$ and two orthogonal excited states $|Y\rangle = \frac{|\downarrow\Uparrow\rangle+|\uparrow\Downarrow\rangle}{\sqrt{2}}$ and $|X\rangle = \frac{|\downarrow\Uparrow\rangle-|\uparrow\Downarrow\rangle}{\sqrt{2}}$, which are superpositions of an electron and a hole pair. Because the QD is not symmetrical due to the growth process (more about this in Chapter 2), the two excited states are non-degenerate and are split by an energy difference of δ. The transitions are referred to as the x- and y-dipole. By singling out one of the dipoles the QD serves as a TLS. In reality however

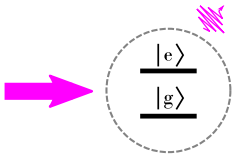

Figure 1.1: A two-level system consisting of the ground state $|g\rangle$ and the excited state $|e\rangle$ being probed by a classical laser on resonance with the transition and emitting a non-classical wavepacket.

treating the QD as a TLS is an approximation as it consists of an infinite set of bound states. The justification is that we will consider near-resonant interactions, so that the transitions to other levels are negligible. Experimentally this can be difficult to achieve as the QD might consist of multiple other levels including the presence of dark states close to resonance, which suppresses the intrinsic efficiency of the system by making it deviate from the ideal case [6]. However, by for example coupling well to only one dipole or by solely collecting the emission from one dipole (e.g. through spectral filtering) the approximation to a TLS is still valid.

Spontaneous emission as described above then occurs because the electron-hole pair recombines by emission of a photon.

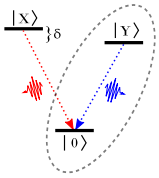

Figure 1.2: Energy levels of the neutral exciton of an asymmetric QD, where the energy difference between the two orthogonal dipoles $|Y\rangle$ and $|X\rangle$ is δ.

1.2 Light-Matter Interaction

In order to better understand the light-matter interaction we describe the system by the Hamiltonian:

$$\hat{H} = \hat{H}_{TLS} + \hat{H}_{field} + \hat{H}_{int} \tag{1.2}$$

Which consists of the matter, being the TLS which as mentioned serves as an approximation to our quantum dots, the electromagnetic light field and the interaction between the two.

Following the approach of [6] we describe the TLS as:

$$\hat{H}_{TLS} = \hbar\omega_0\hat{\sigma}_z \tag{1.3}$$

where $\hat{\sigma}_z = |e\rangle\langle e| - |g\rangle\langle g|$ is the atomic inversion operator while ω_0 is the transition frequency of the TLS.

The electromagnetic field is described as a harmonic oscillator:

$$\hat{H}_{field} = \hbar\omega\hat{a}^\dagger\hat{a} \tag{1.4}$$

where $\hat{a}$ is the creation operator and $\hat{a}^\dagger$ is the annihilation operator describing the creation/annihilation of a photon and ω is the frequency of the light field. The detuning between the TLS and the field is then $\Delta = \omega - \omega_0$.

The QD is a lot smaller than the wavelength of the light and we can therefore apply the dipole approximation such that the interaction is described by a dipole interacting with

an electric field (note that spatial dependence of the field can be neglected because of this approximation):

$$\hat{H}_{int} = -\vec{d} \cdot \vec{E} \tag{1.5}$$

Where $\vec{d}$ is the atomic dipole operator and $\vec{E}$ is the electric field of the probing laser. In the interaction picture and assuming rotating-wave approximation (RWA) this is then:

$$\hat{H}_{int} = \frac{\hbar\Omega}{2}(\hat{\sigma}\hat{a}^{\dagger}e^{i\omega t} + \hat{\sigma}^{\dagger}\hat{a}e^{-i\omega t}) \tag{1.6}$$

Where $\hat{\sigma} = |g\rangle\langle e|$ and $\hat{\sigma}^{\dagger} = |e\rangle\langle g|$ are the lowering and raising operators for the TLS. and where

$$\Omega = -\frac{\langle g|\, \epsilon \cdot \vec{d}\, |e\rangle\, E_0}{\hbar} \tag{1.7}$$

is the Rabi frequency which is proportional to the amplitude of the light field E_0, and serves as the coupling strength between the TLS and the light field. ϵ is the unit polarization vector of the light field.

The significance of Ω will become clear through investigation of the dynamics of the system. However, before that we sum up the expression for the system Hamiltonian (now in the RWA and in the Schrödinger picture):

$$\hat{H} = \hbar\omega_0\hat{\sigma}_z + \hbar\sum_k \omega_k \hat{a}_k^{\dagger}\hat{a}_k + \frac{\hbar\Omega}{2}\sum_k(\hat{\sigma}\hat{a}_k^{\dagger} + \hat{\sigma}^{\dagger}\hat{a}_k) \tag{1.8}$$

which is now summed over all possible modes k of the light field. This Hamiltonian is also known as the Jaynes-Cummings model. A famous model for describing a TLS interacting with a quantized electric field.

Now equipped with the Hamiltonian describing our system and by recalling from Equation (1.1) that the TLS state can be written as: $|\psi\rangle = c_g|g\rangle + c_e|e\rangle$. We can solve the time-dependent Schrödinger equation:

$$i\hbar\frac{\partial}{\partial t}|\psi\rangle = \hat{H}|\psi\rangle \tag{1.9}$$

For the case of exact resonance ($\Delta = 0$) we are left with a pair of coupled differential equations which general solution is a harmonic oscillator. For the special case that $c_g(0) = 1$ and $c_e(0) = 0$ we can calculate the following expression for the population of the excited state:

$$P_e(t) = |c_e(t)|^2 = \sin^2\left(\frac{1}{2}\Omega t\right) \tag{1.10}$$

The population oscillates between the ground and the excited state with a period of $T = 2\pi/\Omega$. For the case of $\Omega = \pi$ the TLS initially in the ground state would be promoted to the excited state with a unit probability. Such oscillations where the energy is periodically exchanged between the TLS and the light field are known as Rabi oscillations.

For many experiments a powerful pulsed laser beam is required. So since we are working with pulsed excitation the field amplitude E_0 is not constant with time which according to Equation (1.7) makes the Rabi frequency time-dependent. We therefore define the pulse area to be: $\Theta = \int_{-\infty}^{+\infty} dt\ \Omega(t)$

Figure 1.3 shows Rabi oscillations from an experiment where a quantum dot is excited resonantly by a pulsed laser. The model fits well to the data in the beginning of the oscillation up to π-pulse. However, the data do not show pure Rabi oscillations instead the system dampens out. This behaviour is not caught by the simple model and must instead be fitted by a model that includes dampening [7]. This dampening could be due to dephasing because the system interacts with the surrounding environment or power broadening. In this case it is most likely caused by power broadening as the system at hand is very well isolated.

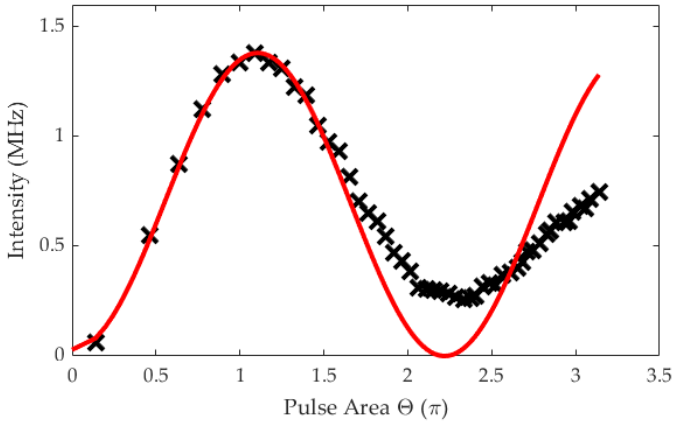

Figure 1.3: Rabi oscillations are achieved experimentally by exciting a quantum dot using a pulsed laser while collecting the resonance fluorescence. The red line is a fit of the simple function in Equation (1.10).

An essential requirement for any work with photons on a quantum level is to enhance and control the light-matter interaction such that an emitted photon couples strongly to one well-defined optical mode [1]. A key parameter describing this is the β-factor, which is the efficiency with which the emitted photons are channeled to the desired mode. Achieving a high β-factor can be realized by embedding emitters in nanostructure containing photonic crystals. This is because of the photonic crystals band gap, which can be engineered in such a way as to strongly suppress leakage to unwanted modes. Furthermore, excitation and collection can be spatially separated by the use of nanobeams which allows for pure collection with only a small amount of laser scattering even when performing resonant excitation, see Figure 1.4. These characteristics make photonic crystal waveguides appealing for realizing efficient single-photon sources.

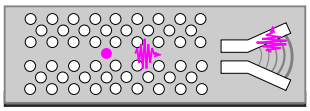

Figure 1.4: Illustration of the structure used for this work. A photonic crystal waveguide, where the photons from the quantum dot are guided to the shallow etched grating out coupling.

This thesis is concerned with generating photons from quantum dots embedded in photonic crystal waveguides and studying the fundamental limits of the quality of the emitted photons and how to overcome the challenges connected to efficient operation of the single-photon source. The quality of a single-photon source can be estimated as how much the generated emission exhibit non-classical behaviour. usually the following parameters are used to qualify the quality of a single-photon source:

- *Purity* of the photons, extracted from a Hanbury-Brown Twiss experiment
- *Indistinguishably* estimated from a Hong-Ou-Mandel measurement
- *Efficiency* of the single-photon source.

These will be described in detail in Chapter 3-4 which explains how to experimentally characterize single-photon sources.

Then follows Chapter 5-7 where it has been investigated how to improve on the quality of the single photon emission by studying the influence that the waterfront and shape of the excitation pulse has on the source.

But before that we must properly introduce how quantum emitters embedded in photonic crystal waveguides are realized as well as a general characterization of the quantum dots.

CHAPTER 2

Quantum Dots in Photonic Crystal Nanostructures

Photons interact very little with their environment and are therefore capable of travelling a great distance with little loss of information. This is essential for information protocols. However, in order to access and control this information, interaction must take place. Hence, it is vital to work with a system where one can enhance the light-matter interaction.

One of the most successful and established platforms for single photon emission are self-assembed InAs quantum dots embedded within a GaAS semiconductor and integrated in a photonic crystal waveguide [1]. Photonic crystal works as cavities enhancing the light-matter coupling while also enhancing the spontaneous emission rate by the Purcell effect. Such a platform has been used for all the work throughout this thesis.

This chapter consists of a brief description of the quantum dots and the nanostructure. Thereafter follows a description of the search and characterization of our quantum dots, where the ordering is made to follow a timeline of how work is conducted in the lab.

2.1 Single-Photon Sources

Most common sources for generating single photons include: spontaneous parametric down-conversion, color centers in diamond, cold atoms, and QDs [5].

Spontaneous parametric down-conversion is a nonlinear optical process where one photon of high energy is split into a pair of photons by a nonlinear crystal. Another approach for generating photons is having a nitrogen vacancy in a diamond, which at room temperature can emit and absorb light.

QDs have the nickname 'artificial atoms' because they behave as a TLS with discrete energy levels, which is excellent for single photon emission as only a single deterministic excitation is active.

QDs do not unlike natural atoms and ions require complex laser cooling and trapping techniques. But they can exhibit a large amount of decoherence due to interaction with the solid-state environment. However, studies into fundamental investigation combined with technological developments in nanofabrication has made it clear that semiconductor QDs are an excellent platform for generating highly efficient pure single photons [8].

Furthermore, semiconductor QDs have a high emission repetition rate, are scalable, and has tailorable optical properties [9]. A challenge that is currently a hot topic for investigation is the fact that semiconductor QDs due to the growth process have a random spatial position [10].

2.1.1 Quantum Dots

QDs can be realized in different ways. Here we work with self-assembled solid state QDs which has been grown by the Stranski-Krastanov method, where InAs is applied on top of a layer of GaAs using molecular beam epitaxy. Because of the difference in lattice constants

between the two semiconducting materials small InAs islands form randomly due to the strain. The confinement results in a 3 dimensional potential, which allows for discrete energy states. These are the QDs, and will generally be asymmetrical with a width of 10-20 nm.

The QDs are embedded in a p-i-n diode structure as can be seen in Figure 2.1a. Surrounding the QD are n- and p-type regions realized by doped GaAs. For further details on the fabrication the reader is referred to [11]. The p-i-n diode allows for control over the electric field across the QDs. Experimentally this is realized by connecting the electrical contacts across the structure to a voltage source. Due to the DC stark effect this results in control over the emission frequency by a few GHz, while also allowing for control over the charges on the QD. The principle of charging the QD is illustrated in Figure 2.1b. By applying a voltage bias across the diode, the slope of the band is lowered allowing the lowest energy level of QD to be below the Fermi level, resulting in a neutral QD (X^0) becoming deterministically charged with a single electron (X^-).

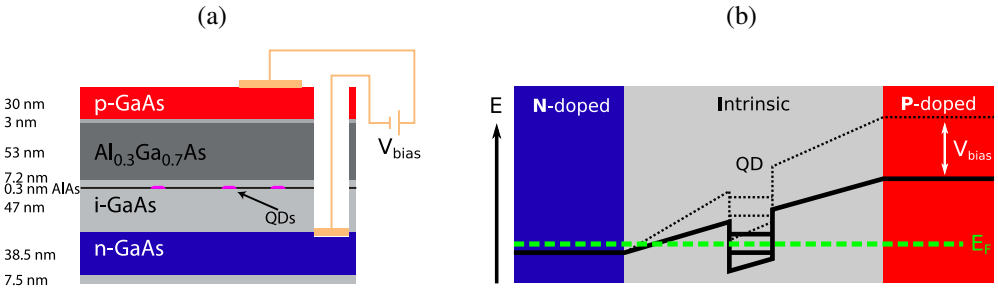

Figure 2.1: (a) Illustration of the p-i-n diode heterostructure. (b) An illustration of deterministic QD charging using a p-i-n diode. The band energy is displayed as a function of the growth direction of the sample. The Red and blue regions represent GaAs containing different doping levels. By applying a voltage bias V_{bias} the energy of a QD conduction band electron is lowered below the Fermi level, leading to a negatively charged QD.

The I-V (current-voltage) characteristics of the diode structure can be seen in Figure 2.2 measured at 1.6 K. The red line is a plot of an ideal diode. We see that the structure exhibits a near ideal I-V curve with only little leakage.

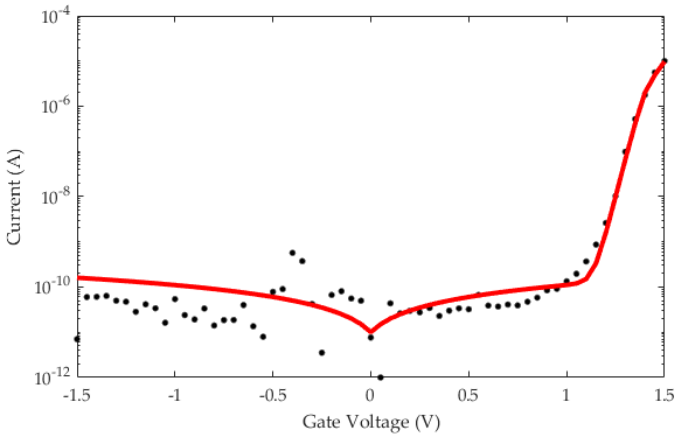

Figure 2.2: I-V characteristics of the diode structure allowing for electrical control over the QD.

2.2 Photonics Crystal Waveguides

As mentioned a key requirement for using QDs as a single-photon source is strong light-matter interaction and the ability to efficiently collect the emitted photons.

This can be achieved by embedding the QDs in a nanostructure. For this work photonic crystal waveguides as seen in Figure 2.3a have been used. The waveguides are engineered in such as way as to decrease the coupling to unwanted radiation modes while increasing the coupling to the desired waveguide mode. The efficiency with which the emitted photons are channeled to the desired mode is the β-factor. This is done by modifying the environment around the QD and thereby, the local density of states (LDOS). This also results in an increase of spontaneous emission rate (the Purcell effect).

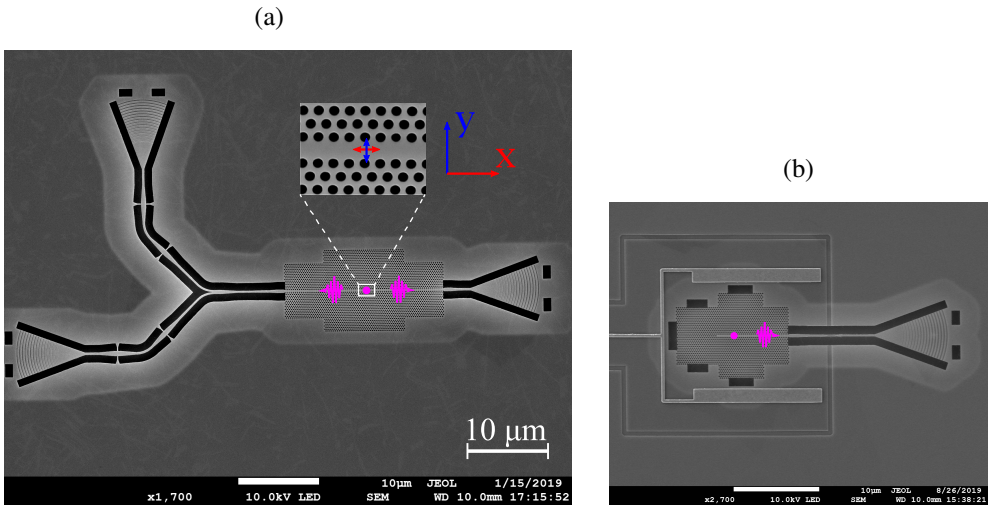

Figure 2.3: SEM of nanostructures. (a) Waveguide with photonic crystal and shallow edge gratings for coupling light in and out of the waveguide. The zoom in shows the coupling of the two dipoles of the QD. The photons emitted from the QD can travel in both directions through the waveguide. (b) More ideal structure for single photon generation as the photonic crystal is terminated by a mirror, so the emission only travels one way.

Recall that the QD had two orthogonal dipoles. The orientation of the dipole moment is defined during the growth process because of the shape asymmetry. Therefore, on a sample the dipoles are oriented along the same axes with some minor variations. The waveguides are then engineered along the same axes as was defined during the growth process. Therefore, to a large degree the dipole orientations of the QD should aligned with either x or y in Figure 2.3a.

The photonic crystal waveguide structure consists of a photonic crystal with a triangular pattern of air holes of lattice constant 248 nm and radius 70 nm. A row without airholes serves as a path. In this specific structure there are three shallow edge gratings for coupling light in and out of the waveguide. This makes it possible to do transmission measurements. Two of them are connected with a y-splitter and nanobeam waveguides.

The efficiency of the waveguides themselves are measured as the propagation loss through the nanobeams. Transmittance of light through the nanobeam waveguide has been measured on nanobeams of varying length. As seen in Figure 2.4 the transmittance decreases exponentially with length.

The nanostructure in Figure 2.3a is designed for transmission measurements, and is not an ideal structure for a single-photon source as 50% of the QD emission is lost when the emission travels opposite the collection grating. This could be solved by eliminating the left side of the structure and having a mirror at the end of the photonic crystal instead (see

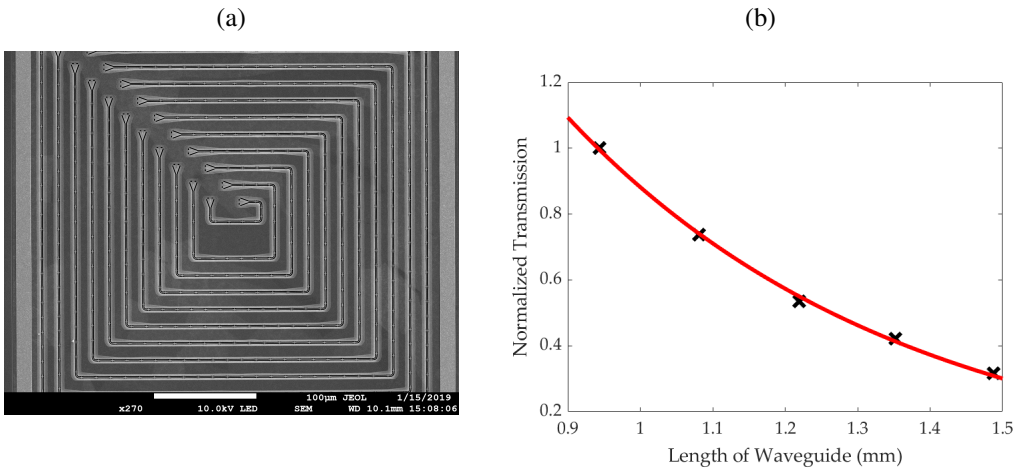

Figure 2.4: (a) SEM of the concentric waveguides of varying lengths used for estimating the propagation loss. (b) Normalized transmission through the concentric waveguides of varying length. The fit is an exponential decay with rate 9.3 ± 0.7 dB/mm.

Figure 2.3b), this would then reflect the photons to the right.

Two main techniques have been used to send light onto the structure. One is resonance transmission (RT) where light is coupled into the waveguide by one of the gratings on the left and outcoupled on the grating to the right. If the frequency of the light is on resonance with the QD the light will reflect and a dip in transmission will be observed.

Another approach is resonance fluorescence (RF), which is the method of choice when using the structure as a source and is illustrated in Figure 2.5. The QD is excited from the top, by sending light down directly onto the photonic crystal. The emission is then collected at the grating to the right. By utilizing this method only a small amount of background laser enters the waveguide.

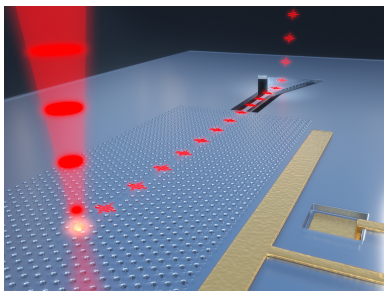

Figure 2.5: Illustration of a QD in a photonic crystal waveguide being excited using the resonance fluorescence technique.

2.3 Quantum Dot Search

Before conducting experiments a QD suiting the requirements for the given purpose must be located and optimized for.

The density of QDs on the wafer depends on the growth process. For this sample the density of QDs were relatively high. This is clear from resonance transmission measurements by scanning over the frequency of the laser as shown in Figure 2.6. The dips in transmission is due to QDs absorbing the laser light when the excitation laser is resonant with the QD transition. The number of dipoles vary largely across structures from around 20 to 70. To determine which QDs are of interest as sources requirements were set. For this

particular structure there are 52 dipoles being excited while only 6 satisfied the following requirements:

- Transmission dip > 60 %
- One pronounced dipole
- Near Lorentzian lineshape
- Close to band edge

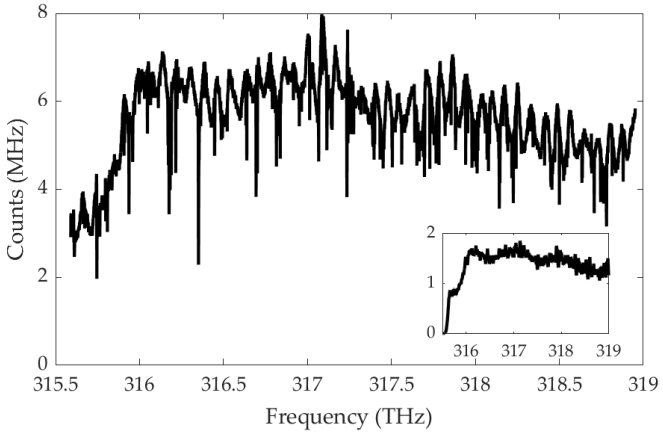

Figure 2.6: Example of resonance transmission when scanning the frequency of the excitation laser from from 315.5 to 319 THz with voltage 1.24 V. The cut-off at 316 THz is a property of the photonic crystal. Each transmission dip is the result of a dipole resonantly absorbing the light. The inset is the 'off-voltage' measurement of 1.00 V, where the QDs are not being excited, essentially showing the laser transmittance.

A large transmission dip suggests a bright dot, well-coupled into the waveguide. If two transmission dips are close together, those might be the two dipoles of the QD. The emission from the two dipoles are distinguishable as they are at slightly different frequencies. To achieve high-indistinguishable photons we only want the emission from one of them, so the emission from the other dipole is often filtered out. Therefore, it is preferred that only one of the dipoles are pronounced as to not lower the source efficiency by exciting the wrong dipole (more on this in Chapter 4). A QD with a single dipole does usually also have a larger transmission dip. Spectral diffusion lowers the efficiency, so it is preferred to have a dipole with a near Lorentzian lineshape. If the transition frequency of the QD is close to the band edge of the photonic crystal the QD is more likely to be Purcell enhanced. Purcell enhancement is the enhancement of the spontaneous emission which increases the rate of the photons.

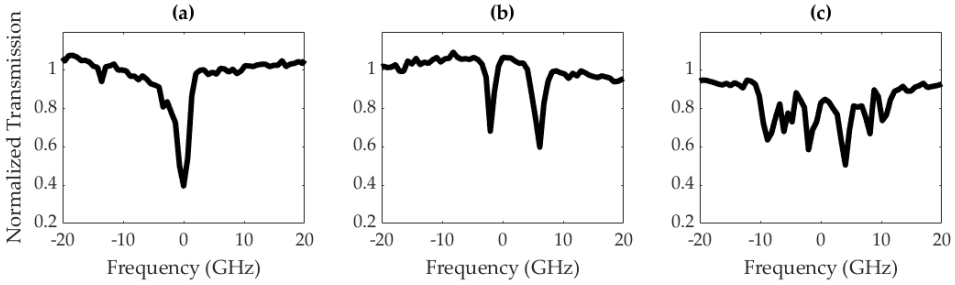

Figure 2.7: Examples of QDs seen in resonance transmission. The intensity is normalized to the background and the x-axis is centered to the peaks. (a) Is the QD that has been characterized in the following section.

Different QD transmission dips can be seen in Figure 2.7, which is a zoom in of some of the transmission dips in Figure 2.6. (a) shows a good candidate where the dip is around 60% only one dipole is present and it sits in a low-noise environment. (b) shows two dips of equal brightness. The two dips could be the two dipoles of a QD being equally excited by the laser. The transmission dip is 40% (c) shows QDs in a high noise environment: The QDs are too close together and deviates from a Lorentzian lineshape, making it a difficult QD to optimize for.

8 photonic crystal waveguide structures have been investigated. The 8 structures contains approximately 350 dipoles, A large amount of the dipoles can easily be discarded as they are simply not bright enough. After assessment 16 QD fills the requirements and are interesting to investigate further from a source perspective.

Ideally one would fit each transmission dip independently using a model such as the one described in [12] to extract not only the transmission dip but also the linewidths of all of the QDs. This has been done for these exact structures in [13].

It should be noted that in a structure designed for source use, where one end of the photonic crystal is terminated, transmission measurements is not possible. That makes the QD search a little more challenging. One approach would be to excite the QDs from the top in RF while moving the position of the beam around in the photonic crystal and scan the frequency. This should ideally be done for different polarizations, which is quite a time consuming method. Another approach would be to send above-band laser through the coupling grating and find QDs based on the reflection.

After the candidates of interest have been selected from the initial transmission scans, we move on to RF. The frequency of the QD is now known from the transmission measurements, so the QD position in the photonic crystal is determined by moving the laser beam across the structure. The QDs are randomly positioned across the whole structure, but we are interested in the ones inside of the photonic crystal as these are Purcell enhanced. So if the QD is not located inside of the photonic crystal or if there is another QD being excited by the light beam at that exact postion the QD is discarded. When a QD has been located inside the photonic crystal, it is optimized for and then characterized as described in the following section. The QD in Figure 2.7a is one of the most interesting candidates and is the one chosen for characterization.

2.4 Quantum Dot Characterization

This section contains general characterization of a neutral charged QD. This investigation is done using the resonance fluorescence method.

2.4.1 Charge Plateau

Figure 2.8a shows the fluorescence when performing a voltage scan using a continuously tunable laser (CTL) at frequency 316.653 THz $\approx$ 947 nm. The X^0 is being resonantly excited. The two dipoles can be observed as the two regions of strong emission at voltage 1.24 V and 1.25 V. The fluorescence fading out until 958 nm is from the phonon sideband. The spike in fluorescence at wavelength 951.5 nm and voltage 1.26 V is from the negatively charged X^- state of the QD, which is indirectly being excited.

A charge plateau of the QD is acquired by exciting the QD with the CTL while scanning the gate voltage and collecting the resonance fluorescence. Such a measurement can be seen in Figure 2.8b where a step size of 0.5 GHz and 0.2 mV is applied and each step is integrated for 0.1 s. The scan shows two plateaus ranging over 80 mV. Control over the voltage gate makes it possible to tune the frequency by around 40 GHz. The two plateaus are the two QD transitions due to the non-degenerate orthogonal dipoles of the neutral exciton. The fine

structure splitting of the dipoles are 6 GHz. The slope is 610 GHz/V which is useful for converting from voltage to frequency as voltage scans in this particular setup can be made with higher resolution.

The plateaus are distinct with the background suppressed making the QD ideal for low-noise operation. At the edges of the plateau the RF falls off due to the QD transitioning from a neutral exciton to a charged exciton. Therefore, operating in the center of the plateau suppressed blinking to other charge transitions. This QDs center frequency is at 316.65 THz with voltage 1.24 V.

As mentioned a neutral charged exciton has two orthogonal dipoles. On the figure below one is more pronounced than the other. This suggests that one dipole is coupled stronger to the waveguide mode (which is along the y-axis if we follow the notation of Figure 2.3a), but also that the polarization of the incoming light mainly excites that dipole. The importance of the overlap between the excitation polarization and the dipole orientation will be further investigated in Chapter 5.

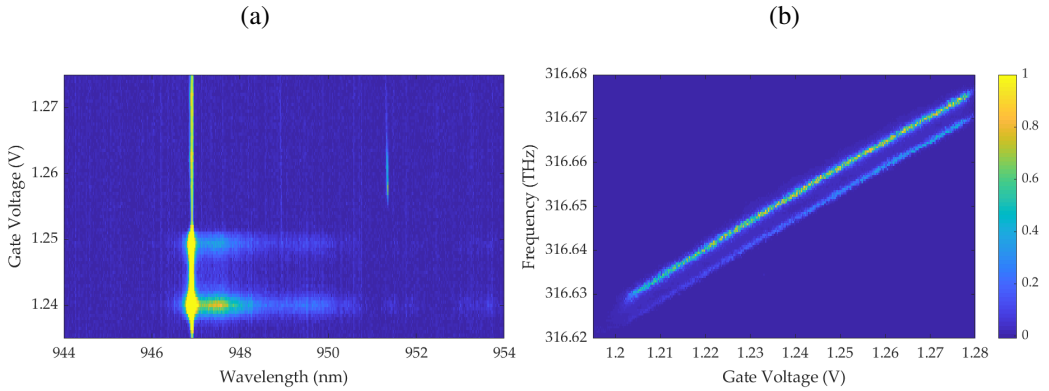

Figure 2.8: (a) Voltage scan when resonantly exciting the X^0 with the CTL. Both the dipoles of the X^0 are visible as well as the X^-. (b) Charge plateau of the QD transition. Resonance fluorescence measured at a power of 0.5 μW while scanning the frequency and gate voltage. The two bright plateaus are the two dipoles of the X^0. The colors are normalized to the max intensity of both plots.

2.4.2 Lineshape

To investigate the lineshape of the QD emission a voltage scan with step size 0.2 mV at the center of the plateau with a frequency of 316.65 THz is performed. The laser is at 0.5 μW and fluorescence is measured for 0.1 s and can be seen in Figure 2.9 where the two dipoles are distinct and the background low.

The lineshape of the QD emission ideally follows a Lorentzian distribution. If spectral diffusion is present the lineshape deviates from the expected result as it broadens due to Gaussian distributed noise. In that situation a Voigt distribution, which is a convolution between a Lorentzian and a Gaussian, would produce a better fit. As can be seen by inspecting the residuals in Figure 2.9 the Voigt fit is close to the Lorentzian implying that the QD is very well-behaved. The FWHM of the y-dipole (left) is 1.88 mV and the x-dipole (right) is 1.95 mV, which in frequency is 1150 MHz and 1190 MHz respectively. The FWHM values are calculated from the Voigt fit.

The emission from a QD contains both the fluorescence from the zero-phonon line and the phonon sideband. This can be observed in Figure 2.10. The phonon sideband roughly follows a Gaussian distribution. When doing measurements a filter is applied to isolate the sideband as well as remove excess laser background.

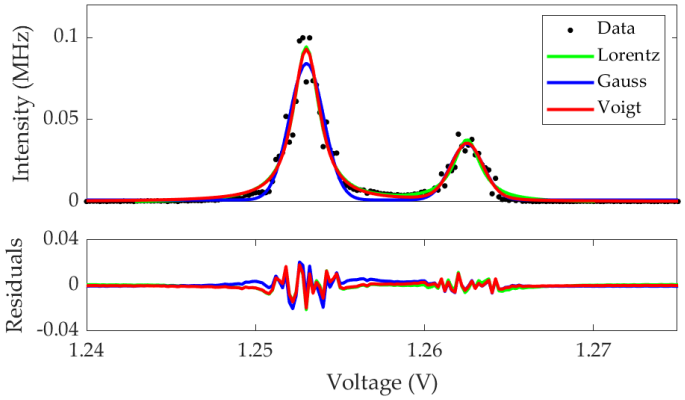

Figure 2.9: Lineshape of the neutral exciton. The measured RF is fitted with 3 different fit models together with the residuals for each fit.

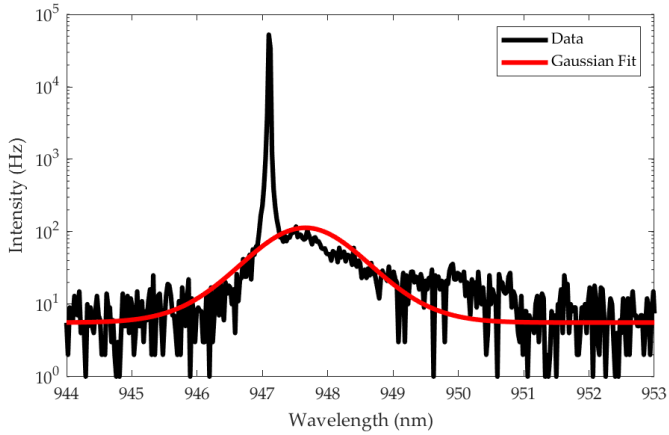

Figure 2.10: Resonance fluorescence recorded on a spectrometer, note the semi-log scale. The zero-phonon line is located at 947.1 nm and the phonon sideband is fitted with a Gaussian distribution.

2.4.3 Lifetime

As expressed earlier a value of interest is the decay rate of the QD, which is related to the lifetime as:

$$\gamma = \frac{1}{\Gamma}$$

The decay rate of the QD emission can be measured by exciting the QD with pulsed laser and using the laser as a reference to time the arrival of the photons. In practice it is done by sending part of the laser directly to a time correlation system, which then compares it to the emission and creates a histogram. *PicoHarp 300* has been used for this purpose. The instrument response function (IRF) is measured by sending weak laser directly to the *PicoHarp 300*. The laser pulses are shorter than the detector resolution rate. So this gives us a measurement of the IRF of the detectors. In Figure 2.11 the lifetime measurement of the two dipoles of the QD can be seen together with the IRF in black. The data are fitted using a convolution between the IRF and a single exponential decay:

$$f(t) = IRF * (p(1) \cdot e^{-\gamma t} + p(2))$$

Where $p(2)$ is the background.

From the fits the decay rate of the two dipoles can be extracted:

$$\gamma_y = 2.874 \pm 0.005\text{ns}^{-1}$$
$$\gamma_x = 1.543 \pm 0.002\text{ns}^{-1}$$

Which translates to a lifetime of $\Gamma_y = 350\text{ps}$ and $\Gamma_x = 650\text{ps}$.

The QD, that has been used as example in this section to show how characterization is performed, meets all the requirements of a well-behaved QD. Other QDs investigated in RF usually behaves similar to the above described.

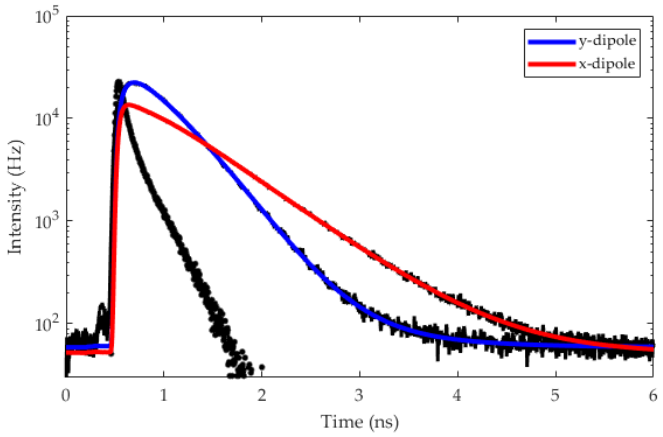

Figure 2.11: Lifetime measurement for the two dipoles of the QD, together with the IRF in black.

We now move onto investigating if the QD also serves as a good single-photon source. This is done through Hanbury Brown-Twiss and Hong-Ou-Mandel measurements.

CHAPTER 3

Characterization Methods for Single-Photon Sources

Characterizing single photons are usually done by measuring the purity and indistinguishability. These measures also serve as main parameters throughout this thesis. They are therefore presented in this chapter from both a theoretical perspective together with a description of the experimental approach for measuring them.

3.1 Hanbury Brown-Twiss

A single-photon source of high-quality should ideally solely emit single photons and not multi-photons. A second-order photon correlation test can characterize the purity of the single-photon source. It gives a measure of the probability that a photon arrives at detector D2 at time $t + \tau$ given that a photon was detected at detector D1 at time t. At time delay $\tau = 0$ we expect no coincidence counts for an ideal single-photon source as only one of the detectors would receive the first event and the system has to be re-excited in order to emit a second photon. This effect is known as photon antibunching, a non-classical effect.

The normalized second-order correlation function can be described by [5]:

$$g^2(t,\tau) = \frac{\langle a^\dagger(t)a^\dagger(t+\tau)a(t+\tau)a(t)\rangle}{\langle a^\dagger(t)a(t)\rangle\langle a^\dagger(t+\tau)a(t+\tau)\rangle} \tag{3.1}$$

For classical light $g^2(t,\tau) \leq 1$ and $g^2(t,\tau) \geq g^2(0)$. However, for quantum light these are both violated.

The Hanbury Brown-Twiss (HBT) measurement is a second-order correlation measurement and can be used to measure the purity. The setup for performing a HBT-measurement can be seen in Figure 3.1. The signal is sent onto a 50/50 fiber beam splitter with the output going into two superconducting nanowire single-photon detectors (SNSPDs). One of the detectors work as a reference. The detected photons are then time correlated using a *Swabian Instruments* Time Tagger which bins the coincidence counts and creates a histogram of detected events. The histogram can then be normalized to a value for large τ where all memory of the first reference event will be lost so that $g^2(\tau = \infty) = 1$. The normalized histogram is a measurement of the second-order correlation function.

Probing the source using a pulsed excitation laser results in distinct peaks in the HBT-measurements separated by the repetition rate of the laser as seen in Figure 3.2a.

The area of the center peak is an estimate of the purity. If the center peak is missing, that is if $g^2(0) = 0$, that signifies ideal pure single photon emission. However, in reality there is often a small peak at $\tau = 0$ for even the most pure single-photon sources.

The $g^2(0)$ can be extracted from the HBT-measurement by integrating the normalized coincidence counts from under the center peak. However, for low counts or small $g^2(0)$ the peak might be limited by the background, which results in an overestimation of the $g^2(0)$. A more robust method is to fit the peak using a convolution between a Gaussian function,

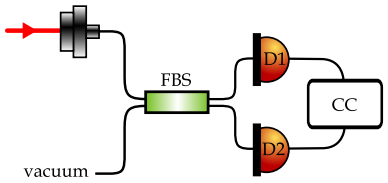

Figure 3.1: Illustration of the HBT setup. The emission is sent through a fiber beam splitter (FBS) and the output is then measured by the two SNSPDs and send to a time tagger for correlation.

which arises from the detectors instrument response function (IRF), and an exponential decaying function.

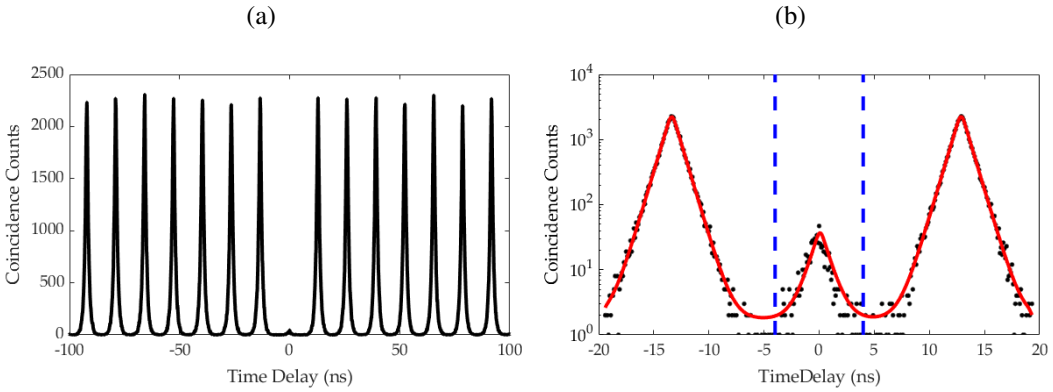

Figure 3.2: Coincidence counts from a HBT-measurement. (a) The peaks are separated by the repetition rate of the pulsed laser. The small center peak at $\tau = 0$ is indicative of the pure emission. (b) Same data as presented on the left panel, but on a semi-log scale. The x-axis is displayed so only the center peak and the peaks beside it is seen. The red line is the fitted convolution. The dotted blue lines marks the window under which the counts are integrated.

In Figure 3.2b the data are plotted on a semi-logarithmic scale which makes it easier to see the center peak. The red line is the convoluted function fitted to the data. Not only is the center peak fitted but also the peaks beside it. This is done in order to fit the background better and make sure that the tails of the peaks beside the center peaks do not influence the extraction of $g^2(0)$. The vertical blue lines show a 4 ns time window of which the counts are integrated under. For longer timescales the center peak starts to become limited by background and the tails from the side peaks. χ^2 is calculated to make sure the fits are reasonable.

Integrating the coincidence counts within a 4 ns window and normalizing to a peak far away results in: $g^2(0) = 0.0165 \pm 0.006$. While the fitting method gives: $g^2(0) = 0.0154 \pm 0.006$. The uncertainties are from assuming the noise to behave Poisson-distributed and by applying error propagation.

The described method of fitting will be used for estimating $g^2(0)$ throughout the rest of this thesis unless otherwise stated.

3.2 Hong-Ou-Mandel

Indistinguishability is a measure of how much the wavepackets of two photons overlap with each other [14]. The Hong-Ou-Mandel (HOM) measurement can be used to get a measure of the indistinguishability of the emission. The original HOM experiment was set to describe the time interval between two photons. The method was reported in 1987 by Hong,

Ou, and Mandel [15] where two photons, the signal and the idler photon, are directed onto a beam splitter where they interfere and are then detected by two photodetectors. Information about the indistinguishability, as well as the photon wavepacket, and the emission lifetime can be extracted from such a measurement [16].

This approach has later become an established technique for measuring the indistinguishably of photons.

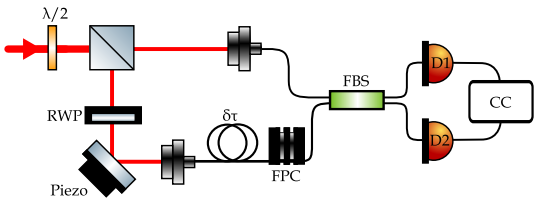

Figure 3.3: Illustration of the HOM setup. The emission is split into two arms. The lower arm delays the emission by $\delta\tau$, before the two paths are interfered at the fiber beam splitter (FBS) and time correlated by the time tagger.

The setup for a HOM measurement can be approach in different ways. For this work it has been accomplished as seen in Figure 3.3. The emission is sent onto a interferometer in a type of Mach–Zehnder configuration. The emission is first sent through a rotatable half-wave plate before being split into two arms by a polarizing beam splitter. These combined serve as a beamsplitter with tunable splitting ratio. The upper arm is the short path were the emission is send straight into a fiber coupler and through the fiber beam splitter (FBS).

In the long path the emission is first sent through a motorized rotating wave plate (RWP) then reflected of a piezo which just serves as a mirror when doing measurements. The emission is coupled into a fiber where a delay of $\delta\tau$ is introduced with respect to the other arm. The delay $\delta\tau$ corresponds to the repetition rate of the laser, so that if the first photon entering the setup is travelling along the long arm and a following photon travels along the short arm, the two photons will arrive at the fiber beam splitter simultaneously. To ensure well-resolved peaks, the delay is chosen to be significantly larger than both the lifetime of the emitter and the detector response time.

Fiber paddles (FPC) are used to control the polarization to ensure that the polarization of the two arms is matching at the fiber beam splitter, this is done pre-measurement.

After the fiber beam splitter the signal is send onto two SNSPDs and time correlated in the same manner as for the HBT-measurement.

Pre-measurement the HOM setup has to be prepared to ensure maximum interference. This is done by sending continuous wave laser through the HOM setup. One of the outputs from the fiber beam splitter is fed as signal to an oscilloscope, the other output is fed to a power meter. Using the half-wave plate the intensity ratio between the two paths is balanced so that both detectors receive the same intensity. This maximises the outcome, and is done by blocking either of the paths and checking the power meter. Then the polarization is adjusted using the fiber paddle to give maximal interference. This is done by using the fiber paddles together with the piezo when balancing the HOM setup before measurements. The piezo is connected to a signal generator and fed as reference to the oscilloscope. The oscilloscope will display the intensity of classical interference fringes of the setup which can be controlled by the fiber paddles.

After this, the setup is prepared and the measurement can be performed for some integration time. A typical measurement is run twice where the RWP has been rotated by 45 degrees. This change in configuration makes the input at the fiber beam splitter either co- or cross-polarized, resulting in either maximally or minimally indistinguishable photons.

The time tagger creates time correlated histograms of the coincidence counts similar to that for the HBT-measurement: If detector D1 measures a photon at time t and detector D2 detects another photon at time $t + \tau$ that signifies a coincidence. Now for $\tau = 0$ the probability of detecting coincidence counts vanishes given that the photons are perfectly indistinguishable [15][16]. This is a known behaviour of a two-photon interference experiment where two photons collide on a 50/50 beam splitter. When the two photons are perfectly indistinguishable they will always exit the beam splitter through the same output port. If the photons become more distinguishable the probability of them exiting different output ports increases. The mathematical description of this is introduced in the next section.

The visibility of the center peak is calculated by comparing the areas of the peak for the co- and cross-polarized cases allowing extracting of the raw visibility according to [17]:

$$V_{raw} = \frac{A_{\perp} - A_{\parallel}}{A_{\perp}} \tag{3.2}$$

Where $A_{\parallel}$ and $A_{\perp}$ are the integrated coincidence counts at $\tau = 0$ for the co- and cross-polarized cases respectively.

The analysis is done in a similar fashion as describe for the $g^2(0)$, where the area under the peaks can be extracted by normalizing to a peak far away where the memory of the first event is gone and integrating the coincidence counts. However, a more reliable approach is to fit using a convolution between the Gaussian IRF and an exponential decay to make sure that we do not miss the tail of exponential in the background the peaks beside the center peak are fitted as well. An example of a HOM measurement is seen in Figure 3.4 where the red fit is for the co-polarized case and the green line is fitted to the cross-polarized data. The dotted blue lines at ± 1.5 ns marks the integration window.

The fitting approach results in $V = 90 \pm 1\%$ while integrating the counts results in $V = 88 \pm 1\%$. The HOM measurements reported in this work are performed at π-pulse unless otherwise stated and fitting is used to extract the visibility.

The center peak of a HOM measurement might broaden resembling a Gaussian lineshape. This is due to dephasing caused by phonons from the semiconducting materials.

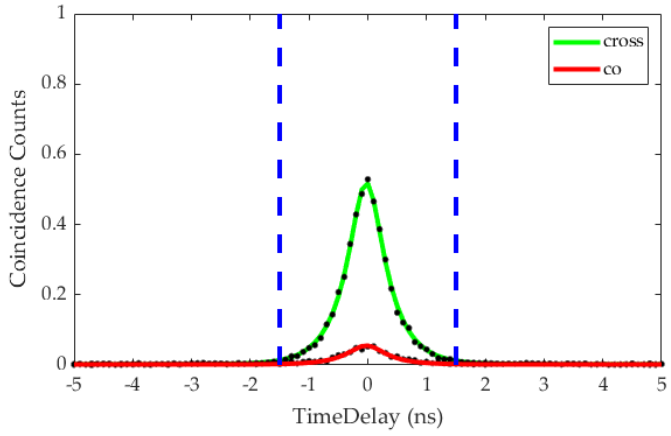

Figure 3.4: Fitted coincidence counts of a HOM measurement for co-polarized (red) and cross-polarized (green) configurations. The x-axis is displayed so only the center peak is seen, however the fits includes the peaks beside the center peak. The dotted blue lines marks the window under which the counts are integrated.

So, from the HOM measurement we directly extract the visibility according to Equation (3.2) which is a direct measure of the indistinguishability as will become clear in the following section.

3.2.1 Indistinguishability

To define indistinguishability we must consider the dynamics happening at the beam splitter. For this we must define some notation[18] and we keep everything as general as possible to begin with.

The beam splitter can mathematically be represented by the transformation matrix:

$$\begin{pmatrix} \hat{c} \\ \hat{d} \end{pmatrix} = \begin{pmatrix} t' & r \\ r' & t \end{pmatrix} \begin{pmatrix} \hat{a} \\ \hat{b} \end{pmatrix} \tag{3.3}$$

with $\hat{c}$ and $\hat{d}$ being the output modes and $\hat{a}$ and $\hat{b}$ being the input modes see Figure 3.5. For which the following relations are satisfied:

$$|r'| = |r|, |t'| = |t|, |r|^2 + |t|^2 = 1, r^*t' + r't^* = 0, r^*t + r't'^* = 0 \tag{3.4}$$

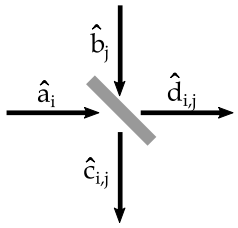

Figure 3.5: Sketch of beam splitter. $\hat{a}_i$ and $\hat{b}_j$ are the input modes while $\hat{c}_{ij}$ and $\hat{d}_{ij}$ are the output modes consisting of a superposition of i and j.

Next the coefficients above are chosen in terms of the transmittance T and reflectance R of the beam splitter, for which $R + T = 1$.

$$t' = t = \sqrt{T}, r' = r = e^{i\phi}\sqrt{R} \tag{3.5}$$

From this we arrive at the beam splitter relations:

$$\hat{a}_i^\dagger = e^{i\phi}\sqrt{R}\hat{c}_i^\dagger + \sqrt{T}\hat{d}_i^\dagger \tag{3.6}$$

$$\hat{b}_j^\dagger = \sqrt{T}\hat{c}_j^\dagger + e^{i\phi}\sqrt{R}\hat{d}_j^\dagger \tag{3.7}$$

We have a phase shift between the transmitted and reflected beams of $\phi = \pi/2$ resulting in an overall phase shift of i between the reflected and transmitted parts:

$$\hat{a}_i^\dagger = i\sqrt{R}\hat{c}_i^\dagger + \sqrt{T}\hat{d}_i^\dagger \tag{3.8}$$

$$\hat{b}_j^\dagger = \sqrt{T}\hat{c}_j^\dagger + i\sqrt{R}\hat{d}_j^\dagger \tag{3.9}$$

As shown in Figure 3.5 we identify the input modes as $\hat{a}_i$ and $\hat{b}_j$ and the two output modes as being superpositions of these: $\hat{c}_{ij}$ and $\hat{d}_{ij}$.

Furthermore, $\hat{a}_i^\dagger$ and $\hat{b}_j^\dagger$ denote the photon creation operator in the two input modes of the beam splitter. While $\hat{c}_{ij}^\dagger$ and $\hat{d}_{ij}^\dagger$ are the creation operators of the output modes. All is defined in the Hilbert space and satisfies the following commutation relation: $[\hat{x}_i, \hat{x}_j^\dagger] = \delta(i - j)$

Now we consider two photons simultaneously arriving at the beam splitter in different modes i and j. These different modes could be different polarization or arrival times [19].

$$|\psi_{in}\rangle = |1_i, 1_j\rangle = \hat{a}_i^\dagger \hat{b}_j^\dagger |\emptyset\rangle \tag{3.10}$$

Where we let $|\emptyset\rangle$ denote the vacuum state. By applying Equation (3.8) and (3.9) we obtain the output of the beam splitter:

$$|\psi_{in}\rangle \xrightarrow{BS} |\psi_{out}\rangle \tag{3.11}$$

$$\psi_{out} = (i\sqrt{R}\hat{c}_i^\dagger + \sqrt{T}\hat{d}_i^\dagger)(\sqrt{T}\hat{c}_j^\dagger + i\sqrt{R}\hat{d}_j^\dagger)\,|\emptyset\rangle \tag{3.12}$$

$$= (i\sqrt{RT}\hat{c}_i^\dagger\hat{c}_j^\dagger - R\hat{c}_i^\dagger\hat{d}_j^\dagger + T\hat{d}_i^\dagger\hat{c}_j^\dagger + i\sqrt{RT}\hat{d}_i^\dagger\hat{d}_j^\dagger)\,|\emptyset\rangle \tag{3.13}$$

Now it is fruitful for clarity's sake to take a short step back from the generality and consider the case of an ideal 50:50 beam splitter, resulting in $R = T = 1/2$.

$$\psi_{out} = \frac{1}{2}(i\hat{c}_i^\dagger\hat{c}_j^\dagger - \hat{c}_i^\dagger\hat{d}_j^\dagger + \hat{d}_i^\dagger\hat{c}_j^\dagger + i\hat{d}_i^\dagger\hat{d}_j^\dagger)\,|\emptyset\rangle \tag{3.14}$$

If we assume that the two incoming photons are in the same mode $i = j$ (that is they are perfectly indistinguishable), then the output state becomes a superposition:

$$\psi_{out} = \frac{1}{2}(i\hat{c}^\dagger\hat{c}^\dagger - \hat{c}^\dagger\hat{d}^\dagger + \hat{d}^\dagger\hat{c}^\dagger + i\hat{d}^\dagger\hat{d}^\dagger)\,|\emptyset\rangle = \frac{i}{2}(\hat{c}^{\dagger 2} + \hat{d}^{\dagger 2})\,|\emptyset\rangle = \frac{i}{\sqrt{2}}(|2,0\rangle + |0,2\rangle) \tag{3.15}$$

Meaning that the two photons will always bunch together and emerge at either of the two detectors and we never see a coincidence count. Which is in agreement with the short discussion of two-photon interference presented in the previous section. (Here it has been used that $\hat{a}^\dagger\,|n\rangle = \sqrt{1+n}\,|n+1\rangle$).

The reason for this outcome can be understood intuitively by considering Figure 3.6, which illustrates the four different paths that the two photons may travel.

For the two middle paths we have a coincidence count. This happens in the process where both photons are transmitted and the process where both photons are reflected. However, these two cases are indistinguishable and interfere destructively with each other due to the phase shift of the beam splitter resulting in zero probability of the outcome that we would have a photon in each detector. On the other hand the other two paths are completely distinguishable, they do not interfere and result in bunching the two photons together at the output states.

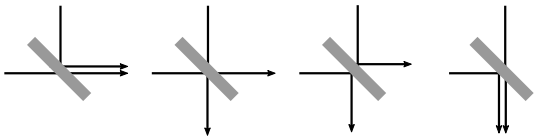

Figure 3.6: The four different paths that two photons entering a beamsplitter may travel.

Going back to the general description we had from Equation (3.13). We are now only interested in the coincidence counts cc, which is the part where one photon is created in both outputs so that both detectors click, that being the two middle terms of Equation (3.13):

$$|\psi_{out}^{cc}\rangle = (-R\hat{c}_i^\dagger\hat{d}_j^\dagger + T\hat{d}_i^\dagger\hat{c}_j^\dagger)\,|\emptyset\rangle \tag{3.16}$$

We can now calculate the probability for coincidence counts as the expectation value:

$$P_{cc} = \langle\psi_{out}^{cc}|\psi_{out}^{cc}\rangle \tag{3.17}$$

$$= \langle\emptyset|\,(-R\hat{c}_i\hat{d}_j + T\hat{d}_i\hat{c}_j)(-R\hat{c}_i^\dagger\hat{d}_j^\dagger + T\hat{d}_i^\dagger\hat{c}_j^\dagger)\,|\emptyset\rangle \tag{3.18}$$

$$= R^2\langle\hat{c}_i\hat{c}_i^\dagger\rangle\langle\hat{d}_j\hat{d}_j^\dagger\rangle - RT\langle\hat{c}_i\hat{c}_j^\dagger\rangle\langle\hat{d}_j\hat{d}_i^\dagger\rangle - RT\langle\hat{c}_j\hat{c}_i^\dagger\rangle\langle\hat{d}_i\hat{d}_j^\dagger\rangle + T^2\langle\hat{d}_i\hat{d}_i^\dagger\rangle\langle\hat{c}_j\hat{c}_j^\dagger\rangle \tag{3.19}$$

Now using $\langle \hat{a}_i \hat{a}_j^\dagger \rangle = \delta_{ij}$ where δ_{ij} is the Kronecker delta, and defining the overlap between the two modes i and j as the indistinguishability between them: $\langle \hat{f}_i \hat{f}_j \rangle$ where $0 \leq \langle \hat{f}_i \hat{f}_j \rangle \leq 1$, we are left with:

$$P_{cc} = R^2 + T^2 - 2RT|\langle f_i|f_j\rangle|^2 \tag{3.20}$$

We recall that the visibility was calculated (Equation (3.2)) as:

$$V_{raw} = \frac{A_\perp - A_\parallel}{A_\perp} \tag{3.21}$$

where $A_\perp$ is the cross-polarized case. $A_\perp$ then corresponds to the distinguishable limit being:

$$P_{cc}^{max} = P_{cc}(\langle f_i|f_j\rangle = 0) = R^2 + T^2 \tag{3.22}$$

Which for $R = T = \frac{1}{2}$ makes $P_{cc}^{max} = \frac{1}{2}$ which is exactly what we saw for the cross-polarized case in Figure 3.4. The visibility of the photons can be calculated as:

$$V_{raw} = \frac{P_{cc}^{max} - P_{cc}}{P_{cc}^{max}} = \frac{2RT|\langle f_i|f_j\rangle|^2}{R^2 + T^2} \tag{3.23}$$

For the ideal 50/50 beam splitter we see that $\langle \hat{f}_i \hat{f}_j \rangle$ is in fact the indisinguishability and is equal to the visibility:

$$V_{raw} = |\langle f_i|f_j\rangle|^2 \tag{3.24}$$

3.2.2 Visibility Correction

The measured visibility V_{raw} extracted from the HOM measurement is affected by the performance of the interferometer used to measure it. To extract a more fair estimate the imperfections should be accounted for. Usually there are made three main corrections [14][20]:

1) How the beam splitter ratio deviates from the ideal 50/50. 2) The contrast of the classical interference visibility $(1 - \epsilon)$. 3) The source not being an ideal single-photon source, resulting in a non-zero $g^2(0)$.

The presence of a non-zero $g^2(0)$ is an intrinsic property of the single-photon source and not an artifact of measurement imperfections. Therefore the visibility will not be corrected for $g^2(0)$. However, the $g^2(0)$ dependence on visibility is interesting and will be discussed in Chapter 6.

From Equation (3.23) the influence of any beam splitter asymmetry can directly be extracted by normalizing the raw visibility to the ideal case. Combining this with the correction of the classical interferometer we can extract a more true estimate of the visibility [20]:

$$V = \frac{R^2 + T^2}{2(1-\epsilon)^2 RT} V_{raw} \tag{3.25}$$

Where R and T are the actual beam splitter ratios and $(1 - \epsilon)$ is the fringe contrast.

This correction is used through this thesis. The parameters for the corrections are given in Table 3.1 below. The *Correction* column shows the influence of each of the factors on the visibility.

The fringe contrast is the error connected to the classical interferometer setup. It is measured when the HOM setup is prepared by sending a continuously tunable diode laser (CTL) through the setup and reading the fringe maximum and minimum off of the oscilloscope. The max and min are then corrected for the offset and we estimate the fringe contrast as:

$$(1-\epsilon) = \frac{I_{max} - I_{min}}{I_{max} + I_{min}} = 0.998$$

If we assume the CTL to behave as a monochromatic wave, then the classical fringe contrast becomes $\nu = 2\sqrt{RT}$. This value should be considered a lower bound as imperfect power balancing through the two arms together with imperfect polarization matching influences the visibility: $(1-\epsilon) \geq 2\sqrt{RT} = 0.99885$

Parameter	Value	Correction	Measurement Method
$(1-\epsilon)$	0.998	0.4 %	Fringe contrast measurement with CTL
R	0.476	0.5 %	Resonant transmission with CTL
T	0.524	0.5 %	Resonant transmission with CTL

Table 3.1: Table displaying the parameters and values used for HOM correction together with the method of measuring these factors. The correction column is calculated as the effect the parameter has on the corrected value.

Using the correction of Equation (3.25) we find that a better estimate of the indistinguishability is $91 \pm 1\%$.

3.3 Impurity

For a high-quality single-photon source we expect little or no scattering from the excitation laser in the emission.

When sending light E_{in} onto a waveguide, some of the excitation light will excite the QD, which will then emit photons, but some will also scatter of the structure, and can be thought of as a leakage in the system, see Figure 3.7.

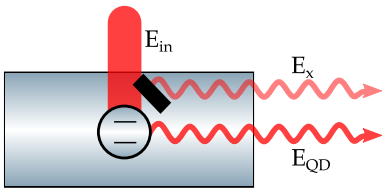

Figure 3.7: Light through the waveguide. Incoming laser from above E_{in} interacts with the QD and with elements (such as phonons) in the waveguide resulting in an output consisting of photons emitted from the QD and scattered laser.

The effective output field is then:

$$E_{out} = E_{QD} + E_x \tag{3.26}$$

where $E_x = E_{in}|x|e^{i\phi}$

$|x|$ is the leakage amplitude and ϕ is the relative phase factor between the incoming light and the scattered light.

To estimate the efficiency of the source we define the impurity as the amount of background laser, compared to the QD emission.

$$\xi = \frac{E_{in}|x|e^{i\phi}}{E_{QD}} \tag{3.27}$$

Under ideal conditions the leakage factor would be zero: $|x| = 0 \Rightarrow \xi = 0$. Zero impurity signifies that each laser photon entering the waveguide either creates exactly one QD photon or exits the waveguide through another mode than the waveguide mode.

The impurity can be experimentally calculated by measuring the intensity of the emission I_{on} and the background I_{off}.

The laser background is measured by tuning the voltage off the QD so the QD is not being excited and then measure the background for some integration time.

The QD emission can be measured as the emission intensity from which the laser background is subtracted. Making it possible to calculate impurity as:

$$\xi = \frac{I_{off}}{I_{on} - I_{off}} \tag{3.28}$$

Instead of just one measurement at an arbitrary power, it is usually preferred to do a power series, where the counts are measured while scanning the power of the excitation laser for an integration time of at least 0.1 s for each step. This also allows for impurity to be measured at π-pulse which is usually where the single-photon source would be operated.

An example of this can be seen in Figure 4.6 where the emission data have been fitted to a Rabi curve (Equation (1.10)). While the background increases linearly with power, see Figure 3.8b. For this specific data set π-pulse is reached at $1.24\mu W$ where $\xi = 0.008$.

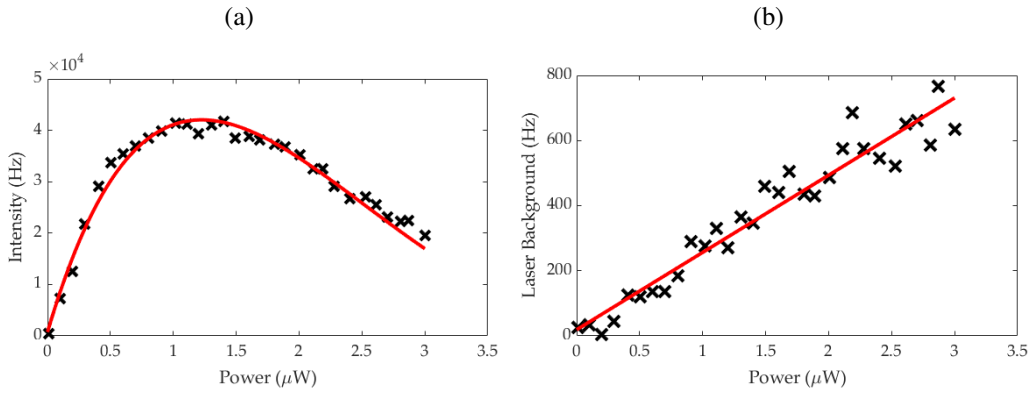

Figure 3.8: Powerseries with fit. (a) Is the QD emission measured at voltage: $V = 1.238V$ and fitted Rabi curve fit. π-pulse is at 1.24 μW (b) Laser background measured at voltage: $V = 1.2V$. Far from the QD dipoles (see Figure 2.9).

The impurity can be related to the $g^2(0)$ by assuming that the QD emission consists of a mixture of single photons and a small amount of background photons which follow Poisson-distributed statistics. For such a state we can express [21]:

$$g^{(2)}(0) \sim 2\xi - \xi^2 \tag{3.29}$$

A test of this can be seen in Figure 3.9a where the red line is an estimate from the equation above. The data points are from a long HBT- measurement where the impurity changed drastically doing integration time (see Figure 3.9b) By splitting the long data set into segments of 15 min the $g^2(0)$ can be extracted and compared to the impurity.

The impurity is monitored doing the HBT-measurement by turning the voltage off each passing minute and measuring the background. Errors on Figure 3.9a are from Poisson statistics for the y-axis, while the errors on the x-axis are taken as the uncertainty on the mean value of the impurity extracted from the data in Figure 3.9b.

Equation (3.29) fits well with the data for larger impurity. However, for small impurity it seems the estimate is an upper bound. The importance of having a low impurity for a single-photon source is clear. Impurity will at the fundamental limit be limited by phonons of the semiconducting materials.

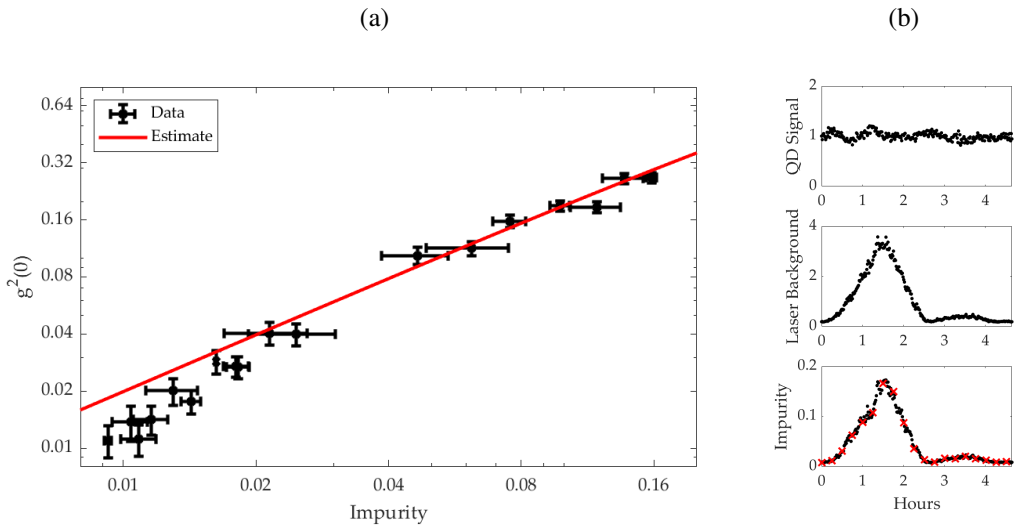

Figure 3.9: (a) Data are from one long 4.5 hour hands-free HBT-measurement, where the $g^2(0)$ worsens as impurity increases. Note the log-log scale. $g^2(0)$ is measured at pulse area π. The red line is an estimation made from Equation (3.29). (b) Monitoring QD emission and background while running the experiment. The top panel shows the QD signal (normalized to the mean) being constant and only showing slow minor variations of 7%. The middle panel shows the laser background. It is clear that the scattering is causing the rise in impurity as seen in the bottom panel. The red crosses marks the interval from where the $g^2(0)$ measurements in (a) are made.

3.3.1 Long Term Stability

A single-photon source might be required to generate high-quality photons for a long duration of time. For this the source impurity should be stable as to avoid a decrease of quality over time.

From Figure 3.9 It should be clear that it is important to monitor impurity. The data are from one long 4.5 hour hands-free HBT-measurement. If one naively uses the entire data set to calculate purity the result is $g^2(0) = 0.077 \pm 0.02$ while a weighted average of the segments gives: $g^2(0) = 0.041 \pm 0.02$.

If one on the other hand extracts the data where impurity is considered optimal. For this case I omit the triangle and thereby discard data from 0 to 2.5 hour. The result is $g^2(0) = 0.019 \pm 0.012$. This shows that the purity can be readily improved by keeping the setup stabilized.

It should be noted that this suggest that many $g^2(0)$ estimates could be upper boundaries.

From Figure 3.9b it is observed that the fall in impurity does not arise from a decrease of counts over time but rather a very small variation due to free optics. This increases the scattering into the waveguide quite a lot as can be seen by the prominent triangle, which is probably the result of a mirror straining and relaxing over more than 2.5 hours. Ways to suppress the laser scatter will be investigated in Chapter 5.

We have now presented the purity and indistinguishability as the two methods used for characterizing single photon emission. However, for sources a third aspect is of great interest: The efficiency of the single-photon source will be investigated in detail in the following chapter.

CHAPTER 4

Single-Photon Source Efficiency

The experimental setups together with the efficiency of the overall system will be described in this chapter.

4.1 Cryostat and Optical Bread Board

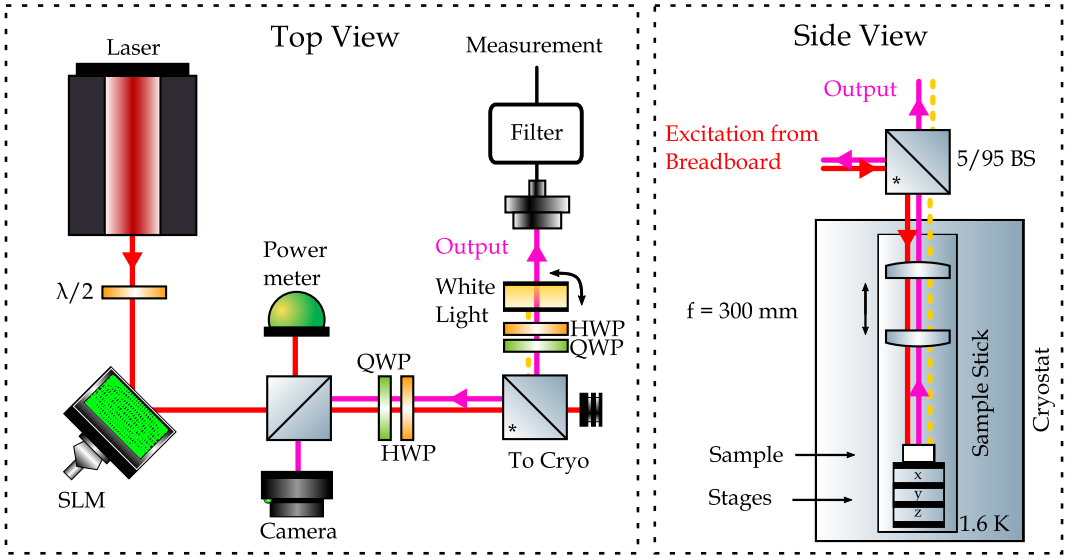

Figure 4.1: Optical bread board for excitation of the quantum dot as well as collection of the single photons. The 5/95 beam splitter '*' indicates where the light is send into the cryostat and is the same on both the top and side view. Red light is the excitation light. The magenta light is the emission from the sample. The dotted yellow light indicates the white light which can be flipped in to allow camera view of the sample.

The optical setup for the single-photon source can be seen in Figure 4.1. To the right is an illustration of the cryostat. The nanostructure is placed in an AttoDry 2100 cryostat which can maintain the sample at a temperature of 1.6K by helium-cooling. The sample is sitting at the bottom of the sample stick which also serves as a vacuum chamber. Below it are three stages that can be moved independently in the xyz directions. The sample is connected to electrical contacts which ensures voltage control. The optical breadboard illustrated to the left in Figure 4.1 is placed on top of the cryostat and ensures optical access to the sample.

Laser light is send onto the breadboard from a fiber coupler where different types of laser can serve as input. The light travels freespace through a wave plate and onto the spectral light modulator (SLM). The SLM can change the phase of the light and the use of this will be discussed in Chapter 5. When the SLM is turned off it serves as a mirror. The light then enters a 50/50 beam splitter. The reflected part is send into a power meter this is

used as feedback for the power control to suppress fluctuations. The transmitted light is send through a quater-wave plate (QWP) and a half-wave plate (HWP) for polarization control of the excitation light. Both wave plates are mounted on motorized rotation stages, so the polarization can be controlled through a computer. There is now achieved full control over both the phase and the polarization of the light which is send through a 9/95 beam splitter and into the sample stick where it is focused onto the sample using two lenses in the focal path $f = 300$mm.

The white light can be flipped into the path so it directs light directly onto the sample. The reflection from this can then be picked up by the camera, so the sample can be visualized.

For collection the light is send upwards out of the structure using shallow edge gratings and travels through the same 5/95 beam splitter as was used for excitation. The choice of a 5/95 beam splitter allows for a greater amount of emission to go to the collection fiber. Part of the emitted light is reflected back onto the breadboard and into the camera.

The output from the 5/95 beam splitter is the QD emission and should be collected efficiently. This output travels through a set of wave plates, which is aligned parallel to the polarization axis of the collection grating, before being collected by a fiber coupler into a single mode fiber. The emission may if so desired be send through a filtering process. We had two spectral filters at disposal: A 3 GHz etalon filter and a 22 GHz grating filter. The output might be send directly to a superconducting nano-wire single photon detector (SNSPD) or through a measurement setup for performing Hanbury-Brown Twiss or Hong-Ou-Mandel measurements.

4.2 Additional Experimental Comments

Any additional comments on the experimental setup is briefly described in this section.

Excitation Lasers

Figure 4.1 shows the input laser directly on the optical breadboard. But in reality there were two laser sources, CTL and MIRA, available and they were connected to the optical breadboard by fiber couplers. The CTL (continously tunable laser) is narrow in bandwidth, and the frequency is easily locked and controlled using a wavemeter in a feedback system. Scanning the laser frequency is very useful for QD searching. The MIRA is much broader in bandwidth and sends out $\sim$4 ps laser pulse at a repetition rate of $\sim$76 MHz. For doing measurements and deterministically driving the single-photon source pulsed laser is preferred.

5/95 Beam Splitter Reflectivity Correction

The beam splitter in collection is effectively a 5/95, which optimizes the collection efficiency. However, the beam splitter transmittance depends on the polarization of the laser, and we want to be sure of exactly how much power we are sending onto the sample. Therefore the beam splitter dependence is corrected for, by sending through laser at 1μW while changing the HWP and QWP and measuring the power after the beam splitter using a power meter. The results of such a measurement can be seen in Figure 4.2. This then serves as a lookup table for future polarization measurements. This ensures that whenever the polarization of the incoming beam is changed the input power is corrected for in relation to the lookup table so that the power on the sample is held constant.

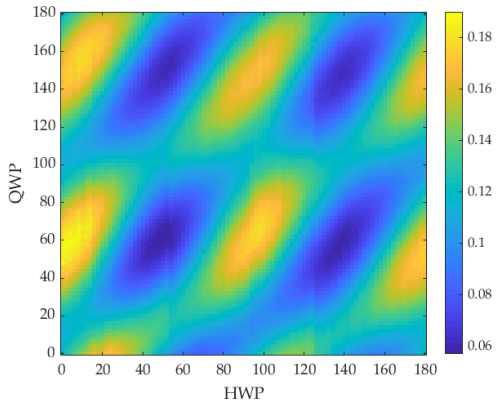

Figure 4.2: Lookup table that corrects for the power dependence of the 5/95 beam splitter. The colorbar is the transmittance normalized to the input power.

Filtering

As mentioned two types of filtering setups were available. A 22 GHz grating filter with an efficiency limited to ∼40% (including fiber couplers). The broad bandwidth is good for filtering out other QDs that are being off-resonantly excited by the laser beam, however it is allowing both dipoles through. The other filter is a narrow bandwidth 3 GHz etalon filter. It has a higher efficiency of 88% (including fiber couplers). However, the allowed frequency is repeated with a spacing of ∼100 GHz, meaning that it might allow some emission through that is spaced 100 GHz away from resonance.

Detection

After filtering (if so desired) the emission is detected using superconducting nanowire single-photon detectors (SNSPDs) and a *Swabian Instruments* time-tagger. The instrument response function (IRF) of the detection setup is measured as to estimate the efficiency as the IRF maps out the incoming photon flux to detected events. This is done by sending weak pulsed laser through the detectors and time-tagger and measuring the events.

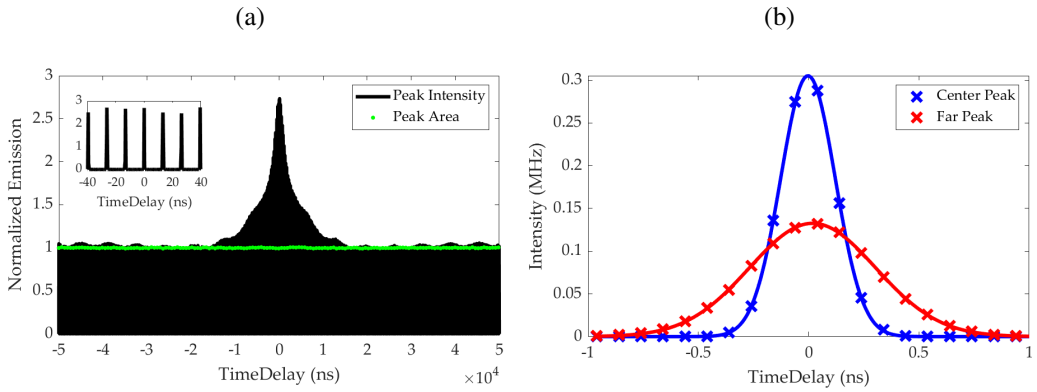

Figure 4.3: (a) IRF for long time scales when using a pulsed laser. Peak amplitude in black while green is the peak areas both normalized to $\tau \to \infty$ It is clear that there is bunching present. The inset shows a zoom in. (b) A center peak and a peak at long timedelay are fitted with a Gaussian function. There is a clear difference in FWHM and amplitude between the two.

Figure 4.3a shows the peak amplitude in black and the area of the peaks in green, both normalized to peaks far away. It is clear from the bunching effect that the time-tagger

introduces internal noise. The bunching was not present when using a *PicoHarp* for time correlation. This intrinsic timing jitter causes great variations in the intensity across long timedelays. The slow oscillations are aliasing due to binning.

Figure 4.3b shows Gaussian fits to two of the peaks. Blue is from the center for $\tau \approx 0ns$ and red is for the peak furthest away at $\tau \approx 50\mu s$. The amplitudes are very different, but the areas of the Gaussian fits are the same, as can be seen by the green data points in Figure 4.3a. This highlights the importance of using the area as a measure for extracting values from for example HBT- and HOM-measurements when working with this detection setup.

Optimization

Operating the single-photon source requires stability across the different systems as illustrated in Figure 4.4. The frequency overlap between the components must be optimized by carefully calibrating every setup in order to maximize the outcome. This also highlights why low spectral diffusion of the QD is desired - if the QD fluctuates too much everything is off.

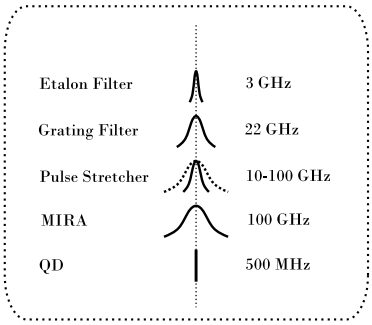

Figure 4.4: Illustration of the different system frequencies that must overlap to ensure that the QD is being optimally excited. Note nothing is drawn to scale. Also the pulse stretcher will be introduced in Chapter 6.

4.3 Efficiency

For a high-quality single-photon source efficiency is an essential merit. The overall efficiency is determined by three main parts: 1) the intrinsic efficiency of the QD as a source, 2) the on-chip efficiency of the photonic crystal waveguide, and 3) the efficiency of the setup. The following is a breakdown of these.

1. Source Efficiency

The intrinsic efficiency of the QD source itself is the probability that the excitation of the QD is emitted into the desired waveguide mode. So the source efficiency can be thought of as:

$$\eta_{QD} = \frac{\gamma_{rad}}{\gamma_{rad} + \gamma_{nrad}} \tag{4.1}$$

Where γ_{rad} is the decay rate into the desired mode, and γ_{nrad} is the intrinsic decay rate into any other modes. γ_{nrad} is difficult to estimate directly [1]. But it can be described by considering which different phenomenons leads to the QD emitter deviating from a TLS.

The QD is operated at a voltage of 1.253 V for a frequency of 316.653 THz, which is in the center of the X^0 charge plateau. This suppresses any blinking to other charge states. As mentioned the X^0 has two orthogonal dipoles spaced approximately 6 GHz apart. For high-indistinguishability we are only interested in the emission from one diople. We choose

the y-dipole as this is orientated along the waveguide. The excitation laser is broad enough in frequency to excite both dipoles, but the emission from the x-dipole is mostly filtered out using the etalon filter. We would assumed that it is preferable if the QD only emitted into the y-dipole in order to increase emission rate. By adjusting the excitation polarization, we can control how much we are exciting either of the dipoles as seen in Figure 4.5 where the voltage is scanned for different polarizations of the excitation laser. We observe how changing the polarization can select how much of each dipole is being excited. For the upper panel the polarization is chosen as to completely suppress the x-dipole, while the bottom panel is the emission from when a combination of both the dipoles are excited (more about this in the following chapter).

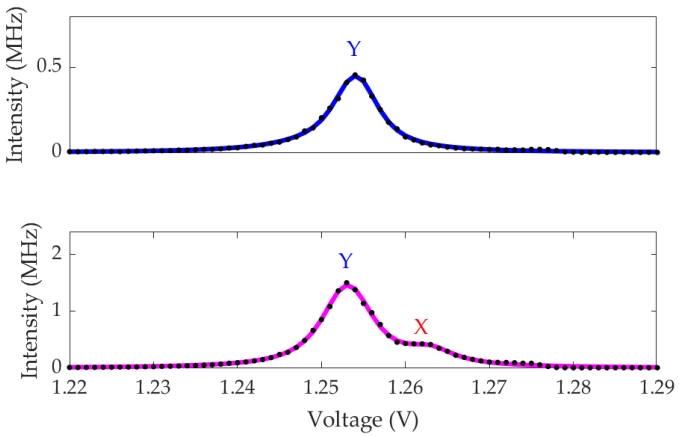

Figure 4.5: Resonance fluorescence when exciting the QD using a pulsed laser of power 1μW and scanning the voltage. Top panel is for the case where the excitation polarization is aligned to the well-coupled y-dipole of the QD. The bottom panel is for another polarization, which is aligned for low impurity. We observe how emission from the x-dipole is now present. The data are fitted using Voigt functions.

The power has been scanned for the two cases, which can be seen in Figure 4.6 where Rabi-curves have been fitted to the data. In Figure 4.6a the x-axis has been normalized to the pulse area π. For Figure 4.6b the x-axis is the power on the sample. The power is measured before the HWP and QWP as was shown in the setup illustration. The path down to the sample contains 4 optical elements of transmittance 98.5% and the objective of transmittance 80%. To calculate the power on the sample the measured power has therefore been corrected by 75.3%. Furthermore, as mentioned in the previous section the 5/95 beam splitter is polarization dependent. So the lookup table in Figure 4.2 has been used to correct for the two different polarizations. The y-dipole (blue) is corrected by 18.23 while the combination dipole (magenta) is corrected by 17.22.

From these fits together with the impurity fits in Figure 4.7 the single photon count rate and the impurity at π has been extracted and can be seen in Table 4.1.

We observe that even though the count rate is slightly larger for the y-dipole polarization the impurity is very large (see Figure 4.7). When the excitation polarization is fully aligned with the y-dipole, the laser couples very well with the waveguide mode, but not at all with the out-of-plane mode which is the mode that the QD is excited through using RF. Therefore a lot more power is needed to reach π which introduces complex scattering. As discussed earlier impurity is a main concern for a high-quality single-photon source and should not be neglected on account of a higher emission rate. When the excitation polarization is chosen as to excite the x-dipole a little (magenta fit) the impurity becomes a lot better. A small adjustment to the polarization so that it excites the QD a little off the well-coupled dipole of the waveguide is therefore desired when utilizing the QD as a source. Therefore the fraction of emission decaying from the x-dipole contributes to the efficiency of the source.

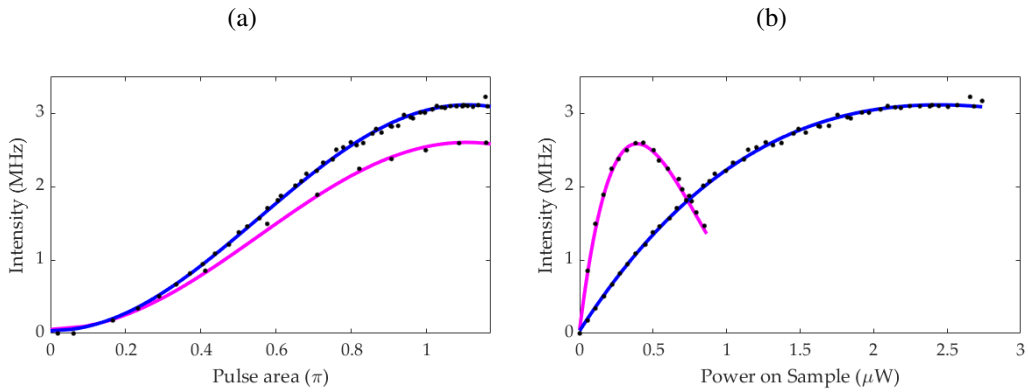

Figure 4.6: Resonance fluorescence at 1.253 V. from power scans from the two different excitation polarizations shown in Figure 4.5. Blue is aligned to the well-coupled y-dipole. Magenta is aligned for low impurity. The data are fitted with a Rabi-curve. (a) The data are normalized to the π-pulse area. The count rate is a little higher for the y-dipole configuration. (b) Same as in (a) but the x-axis is the power send onto the sample. A lot more power is needed to reach π-pulse in the y-dipole configuration.

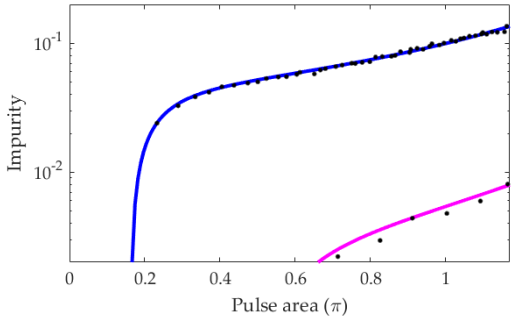

Figure 4.7: Impurity measured from the power scans for the two different excitation polarizations. Blue is aligned to the well-coupled y-dipole. Magenta is aligned for low impurity. The data are normalized to the π-pulse area. The impurity is constantly higher for the y-dipole configuration.

The fraction is calculated from the bottom voltage scan in Figure 4.5. Comparing the areas underneath the two dipoles from the Voigt fits we find that the well-coupled y-dipole is excited with a probability of: $\eta_y = \frac{A_y}{A_y + A_x} = 85\%$. This means that the weaker coupled x-dipole is excited by 15%.

Dipole	Power at π (μW)	Impurity at π	Counts at π (MHz)
Y-dipole	2.39 ± 0.04	0.120 ± 0.003	3.11 ± 0.02
Combination-dipole	0.40 ± 0.06	0.0070 ± 0.0009	2.60 ± 0.03

Table 4.1: Values are extracted from the Rabi-fits in Figure 4.6.

The β-factor is a measure of how well the QD emission is coupled to the waveguide modes. So in this case it is how well the y-dipole is coupled to the waveguide. This number is extracted by fitting the resonant transmission dip using a model described in [12].

As previously mentioned a fraction of the QD emission stems from the phonon sideband which is filtered out in order to generate highly indistinguishable photons. From Figure 2.10 the fraction is calculated to be $\eta_{zpl} = 95 \pm 1\%$.

A small amount of bunching is observed when performing a long time $g^2(0)$-measurement

(see Figure 4.8). This indicates that the QD exhibits a small amount of blinking to other non-radiative dark states doing resonant excitation due to a weak coupling. This contribution can be estimated by modeling a 3-level system system and calculating the dark state population. This has been done in [11] where it is estimated that the probability of the QD to decay to a dark state is 2%, making the probability that the QD decays to the bright state: $\eta_b = 98\%$.

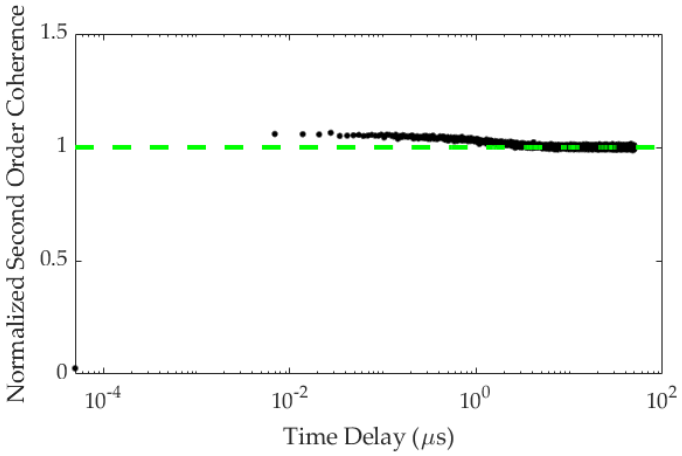

Figure 4.8: Small amount of bunching is observed from the normalized $g^2(0)$ being above 1 for $> \mu$s timescales. The data are from a HBT-measurement where the peak area has been normalized to a peak far away.

2. Waveguide Efficiency

There are also losses connected to the photonic crystal waveguide platform. One of these are the minor propagation losses through the waveguide. It was previously shown (Figure 2.4b) how the transmission through waveguides of varying lengths were measured and the estimated propagation loss was calculated to be 9.3 ± 0.7 dB/mm. The light travels approximately 10 μm from the QD in the photonic crystal to the outcoupling grating. This results in an on-chip efficiency of $\eta_{wg} = 97 \pm 1\%$.

Furthermore, as mentioned the photonic crystal waveguide structures that have been used in this work are designed for transmission measurements and not source generation. The emission can travel in both directions through the waveguide, so 50% of the emission is not being collected.

There are also losses connected to the shallow-edge gratings which outcouples the light from the waveguide. The diffraction efficiency of the shallow-etch grating was estimated to be $\eta_g = 50 \pm 1\%$ [22]. In order to efficiently collect the single photons into a single-mode fiber, the shallow-edge grating must be engineered to optimally mode match the diffracted emission to the fiber mode. The efficiency of this is measured to be $\eta_c = 59 \pm 2\%$ [22].

3. Setup Efficiency

The optical setup can be split into two parts: collection and filtering.

The optical collection efficiency η_{op} is the total efficiency of the optical setup described above: from the sample to the collection fiber. The transmittance through many optical elements contribute to this efficiency including beam splitters, wave plates, and fiber couplers. The transmittance of each optical element used in collection is characterized by measuring the power being transmitted through using the CTL. The sum of efficiency of all components is: $\eta_{op} = 70 \pm 1\%$ [11].

Post collection a 3 GHz etalon filter is employed to collect only the emission into the zero-phonon line by centering the filter to the QD resonance. The transmission through the etalon filter is measured to be $98 \pm 1\%$. This is measured by sending through CTL and using a power meter to check the transmittance. The filtering process includes fiber coupling, which has an efficiency of $90 \pm 1\%$, making the total filter efficiency: $\eta_f = 88 \pm 1\%$.

Total Efficiency

The contribution of all the above mentioned components is summarized in Table 4.2.

	Component	Efficiency
SETUP	* Collection Optics η_{op}	$70 \pm 1\%$
	Etalon Filter η_f	$88 \pm 1\%$
	Setup Efficiency	$62 \pm 1\%$
WAVEGUIDE	On-chip Propagation η_{wg}	$97 \pm 1\%$
	Directionality	50%
	* Shallow-edge grating η_g	$50 \pm 1\%$
	* Waveguide outcoupling η_c	$59 \pm 2\%$
	Waveguide Efficiency	$14 \pm 1\%$
SOURCE	*β-factor	$92 \pm 5\%$
	Zero-phonon line η_{zpl}	$95 \pm 1\%$
	Y-dipole η_y	85%
	Blinking η_b	98%
	Source Efficiency	$73 \pm 5\%$
	Total Efficiency η_{tot}	$6 \pm 1\%$

Table 4.2: Table displaying the efficiencies mentioned above. The efficiency of components marked * are from [11].

The expected rate of single-photon emission can be predicted by:

$$I_{exp} = \eta_{tot}\eta_{det}T \tag{4.2}$$

Where η_{det} is the detection efficiency estimated to $\eta_{det} = 65 \pm 5\%$ in [23] and $T = 76$ MHz is the laser repetition rate.

Expected single-photon rate	3.0 ± 0.7 MHz
Measured single-photon rate	2.60 ± 0.03 MHz

Table 4.3: Comparing the expected rate of emission to the measured emission rate.

Table 4.3 compares the expected single-photon rate to the measured value, which seem in agreement. The measured emission rate is extracted from π-pulse of Figure 4.6.

The total efficiency at the collection fiber is $\eta_{tot} = 6 \pm 1\%$. The main contributor to this value being the non-ideal structure of the waveguide as has already been mentioned. Additionally, the efficiency of the shallow-edge gratings and the collection optics are large factors. These could be majorly improved by employing on-chip fiber couplers, so the collection fiber is directly coupled to the nanostructures which avoids all optical losses [24].

To sum up we are able to generate single photons and have achieved a purity of $g^2(0) = 0.0154 \pm 0.006$ and indistinguishability of $91 \pm 1\%$ with an efficiency of $\eta_{tot} = 6 \pm 1\%$.

We are now interested in how these numbers can be further improved.

CHAPTER 5
Excitation Optimization

It has been studied how the purity can be further improved by optimizing the method for excitation when operating the source. This chapter is dedicated to studying the effect of modifying the wavefront of the excitation laser.

The first part is concerned with the effect that the overlap between the orientation of the QD dipole and the excitation polarization has on the impurity.

The second part is dedicated to studying how laser scattering can be further suppressed by spatial structuring of the phase of the excitation laser. It was previously discussed how the non-zero impurity is largely due to the laser scattering of segments in the waveguide. A way to correct for this scattering would be through phase correction of the incident wavefront. It has been reported how control over the scattered light can be achieved by shaping the spatial wavefront of the incoming laser pulse [25]. In this paper a spatial light modulator (SLM) was used in a feedback system to minimize scattering and thereby optimize the transmission of light through the waveguide. Reporting a technique for optimizing a single-photon source by controlling the polarization as well as the phase of the input laser is the focus of this chapter.

5.1 Polarization Optimization

In Chapter 4 we briefly touched upon the importance of polarization. The optimal excitation polarization for single photon emission turned out to be where a combination of the two dipoles were excited.

As we saw in Figure 4.5 the overlap between the laser excitation polarization and the orientation with the QDs dipoles decides how much of each dipole is being excited and by aligning the excitation polarization we can completely suppress the x-dipole. However, that choice of polarization comes with the cost of higher π-pulse power and higher impurity which is undesirable. This is because the laser is not coupled well to the out-of-plane mode which is how the laser excites the QD in RF.

An attempt to map out the effect that the excitation polarization has on the emission is shown in Figure 5.1. The QD is being resonantly excited. For every 10 degree step from 0 to 100 of the HWP and QWP the power has been scanned to fit the Rabi-curves as in Figure 4.6. The power needed to reach π-pulse has been extracted and the impurity for that power has then been estimated.

As seen in Figure 5.1a more power at the sample is needed for specific polarizations e.g. HWP,QWP = 0,60. This pattern is then repeated by moving the HWP 90 degrees due to its symmetry axis. HWP,QWP = 0,60 corresponds to the y-dipole polarization. As seen in Figure 5.1b and Figure 5.1c The counts are high in that area but that is due to laser scattering as seen by the high impurity.

One could then choose to pick a polarization of HWP,QWP = 70,70 which optimizes to where the impurity is at the lowest. Essentially optimizing for the x-dipole while collecting emission from the y-dipole. But that results in very limited counts.

An optimal polarization for the source would be at around HWP,QWP = 30,50. Here the impurity is low, but the counts are still comfortable. This specific configuration is the magenta colour of the plots in Chapter 4 where the impurity is $\xi = 0.0070$ at π-pulse.

Optimizing the single-photon source impurity by running these extensive mappings is a time demanding process (6-8 hours). A more realistic method for choosing the best polarization is presented: One should excite the QD on resonance with a power well below π-pulse. Then make a coarse scan of the HWP and QWP while measuring the fluorescence. In a $\sim$20 degree proximity of where the counts are comfortably high one should then do a finer polarization scan and choose the HWP,QWP configuration that allows for the smallest impurity.

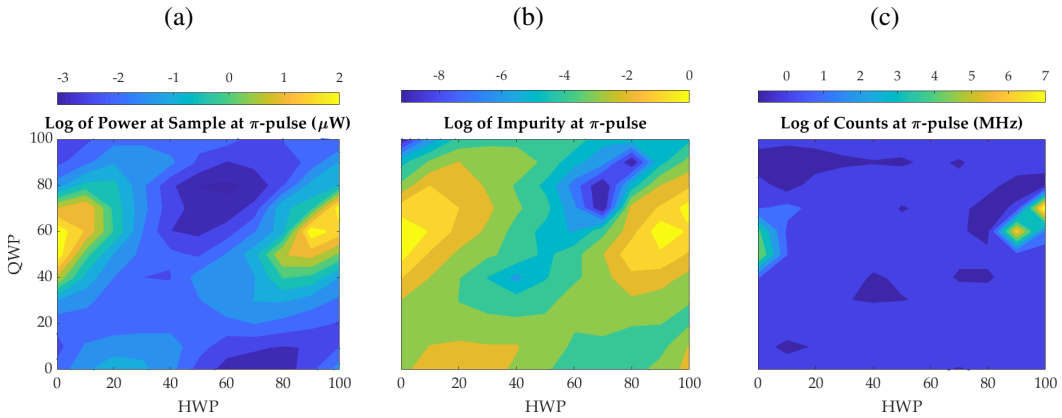

Figure 5.1: Excitation polarization maps at π-pulse. Measured by moving the HWP and QWP in steps of 10 degrees and performing a powerseries. From the powerseries the impurity and counts are extracted by the method described in Chapter 3. Note that all the colorbars are in log-scale. (a) Shows the power at the sample, so these values are corrected for the optics loss and the 5/95 beam splitter dependence. (b) Shows the impurity at π-pulse. (c) Shows the intensity of the QD emission at π-pulse in MHz.

However, it is possible to further lower the scattering, as can also be seen by Figure 5.1b. Therefore, a method for optimizing the impurity directly through phase correction has been studied and is presented in the following.

5.2 Spatial Light Modulation

A SLM can as the name suggests be used to spatially modulate the light beam. This may be utilized to modify the wavefront of the beam by changing the phase, polarization, or the amplitude locally.

Different types of SLM exist that employ liquid crystals, micromirror arrays, or phase-change materials to induce the local change in the phase of a beam. In the current experiment, a liquid-crystal based phase-only SLM (HoloEye Pluto-2 SLM) has been used.

The device consists of a 2D array of 1920x1080 pixels which can be individually programmed to be assigned a value between 0 and 255 equivalent to changing the phase from 0 to 2π by electronic means after appropriate calibration.

To arbitrarily shape the phase front of a beam the full 2π modulation is needed.

The excitation beam is reflected off the SLM as seen in Figure 4.1. The reflected beam is then sent onto the sample as $E_i(t)$, where the phase of the wavefront has been modified via the SLM, adding a controllable phaseshift of $\Delta\Phi_i$ to each of the N pixels.

The total field scattering onto the waveguide $E_{out}(t)$ is therefore given by the sum over all pixels:

$$E_{in}(t) \xrightarrow{SLM} E_{out}(t) = \sum_{i=1}^{N} E_i(t) e^{i\Delta\Phi_i} \tag{5.1}$$

Therefore, optimizing the phase front comes down to finding the values $\Delta\Phi_i$ that allows for the smallest amount of laser scattering into the waveguide mode. This can be done by a machine learning algorithm, that optimizes for the best possible values of $\Delta\Phi_i$. While each pixel can be optimized independently, this is a tedious process given the ~ 0.5 million pixel coverage of the incident laser beam on the SLM. Instead, we chose to approach the wavefront optimization from the perspective of wavefront aberrations that allows us to engineer the shape and local phase within the laser beam spot.

5.2.1 Zernike polynomials

Wavefront aberrations are usually represented mathematically as a series of Zernike polynomials (ZP).

ZP are a sequence of circular orthogonal polynomials defined over the unit circle. They form a complete set and can therefore be used as a basis set in linear combination to represent any given 2D function [26].

The incoming light beam from the laser has a gaussian amplitude profile and a constant phase front. To describe the modulations done to such a 2D circular plane ZP are therefore a good choice.

ZP consist of a radial part $R_n^m(r)$ where R_0 is the radius, and an angular part $e^{im\phi}$ over the azimuthal angle ϕ:

$$Z_n^m(r,\phi) = \sqrt{\frac{n+1}{\pi R^2}} R_n^m(r) \cdot e^{im\phi}$$

$$R_n^m(r) = \sum_{k=0}^{\frac{n-m}{2}} \frac{(-1)^k (n-k)!}{k!(\frac{n+m}{2}-k)!(\frac{n-m}{2}-k)!} \left(\frac{r}{R_0}\right)^{n-2k}$$

Where $-n \leq m \leq n$

In Figure 5.2 the first 6 radial orders of ZP (vertical ordering) are displayed.

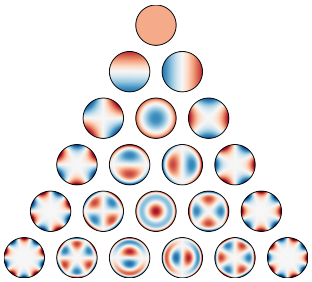

Figure 5.2: Representation of the first 21 Zernike polynomials. Ordered vertically by radial degree and horizontally by azimuthal degree [27].

For the sake of computational time, and because the highest spatial order (which is equivalent to the smallest feature size in the SLM pattern) should not be too large to cause diffraction losses in the setup. It is important to choose the right amount (order) of polynomials to generate. The number of orders is important and should not be raised on account of having fewer iterations [28]. Here a max radial order of $N = 15$ ZP are proposed as a good guidance for optical application. This results in $N_F = (N+1)(N+2)/2 = 136$ functions.

To describe the system a superposition of the ZP are made:

$$F(r,\phi) = \sum_{n=0}^{N} \sum_{m=-n}^{n} \mu_{mn} Z_n^m(r,\phi) \tag{5.2}$$

The optimization then comes down to estimating the coefficients of this linear combination, that is the Zernike moments μ_{kl} that are used as the weights for each of the polynomials.

5.2.2 Machine Learning: SLM for Impurity Optimization

Machine learning can be thought of as an agent interacting with our system through sensors and actuators [29], see Figure 5.3.

It contains a learning algorithm that through a cost function correlates sensor and actuator results and by so learns about the system.

For an agent to be reliable it requires control over the output field E_{out}, which we have through the SLM, as well as a measure for the sensor which we have through detectors by running impurity (ξ) measurements.

The agent then updates its estimation of $\Delta\Phi_k$ for each iteration via the feedback system.

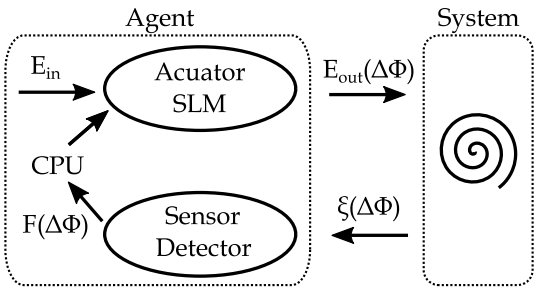

Figure 5.3: Sketch of the feedback system optimizing the wavefront phase.

To optimize the phase of the wavefront for single-photon sources the SLM has been used in reflection as was shown in Figure 4.1. The reflected beam is then sent onto the sample.

The algorithm is programmed in such a way that it for each iteration calculates the impurity and uses this as the cost function. After a given set of iterations the best pattern is then kept. An example of this can be seen in Figure 5.4.

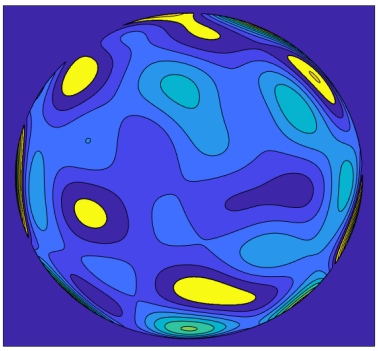

Figure 5.4: An example of a generated phase pattern. The colors corresponds to a phase from 0 to 2π.

5.2.3 Generic Algorithm

Initial Parameters

- The max radial order of ZP that is to be generated: $N = 10$
- Each initial superposition $F_i(r, \phi)$ is a randomly generated pattern. The number of generated superpositions is the population size: $N_{pop} = \sum i = 50$
- The number of iteration runs are chosen as $N_{gen} = 10$. However, one could add a criteria such that the algorithm stops when there is no more improvement between runs.

Iterations

Initial random coefficients are generated for the superpositions $\{F_i(r, \phi)\}$. The impurity is measured for each and they are ranked with the lower impurity getting a smaller rank.

The worst half of the population is discarded. The best half is then used to generate new superpositions. The probability that a particular pattern is picked is weighted by rank, with a lower rank getting a higher weight. This combination of survival and evolution results in faster convergence for large population sizes. The new patterns are then re-ranked together with the best half from earlier.

This process of generating superpositions, measuring the cost function, and ranking the population is carried out for N_{gen} iterations.

When new superpositions are created, a random factor of mutation is added with each generation. This factor decays exponentially as a function of each generation x.

$$K_N = \frac{K_0}{K_E} exp(-\frac{x}{\lambda}) + K_E$$

where $K_0 = 0.15$ is the initial mutation rate, $K_E = 0.008$ is the final mutation rate and $\lambda = 200$ is the decay constant. A random factor is needed so that the optimization process does not get stuck on a local minimum that is different from the global minimum.

In Chapter 3 we discussed how we normally calculate impurity by sending in pulsed light and fitting a power series to extract the impurity at π-pulse. However, this is a slow process that takes close to 1 min and is therefore not the best method for the purpose of machine learning.

Therefore, the impurity in the current experiment has been measured by sending CTL of low power compared to the saturation power P_{sat} onto the sample and then measure the laser background for approx. 2 seconds. The counts should follow a Poisson distribution and a quick fit and extraction of the mean λ_{poi} would suffice for an impurity measurement while the measurement should only take max a few seconds as compared to ~ 1 min. This drastically improves the time it takes to optimize for the best phase pattern. After the pattern has been saved, one can switch to a pulsed laser to conduct further experiments.

Switching lasers might be inconvenient, so an alternative approach would be to use the pulsed excitation laser and go to a low power $P \leq \frac{P_\pi}{5}$ compared to the power at π-pulse P_π, where we are in the linear regime. Then a method similar to that used with CTL could be employed for improving the speed of the algorithm. This approach seems the best but has not been tested.

5.3 Phase Optimization

For the results in this section a negatively charged (X^-) QD with decay rate 1.980 ± 0.004 ns^{-1} has been used.

In Figure 5.5 we see the improvement on the impurity over 10 iterations. The first point at zero iteration, corresponds to no wavefront correction (i.e. diffraction-limited focal spot). The red circles are for a polarization of the incoming laser chosen so as to minimize impurity (corresponding to the magenta plots in Chapter 4) For discussion on the dependence between impurity and excitation polarization recall the earlier section. We see that even for an optimal polarization (in terms of impurity) correcting the phase front still improves the impurity. The blue crosses are for the opposite case, a polarization for which impurity is large. This is achieved by turning the HWP in front of the SLM by 45 degrees. A large improvement by a factor of 10 is seen after just 4 iterations.

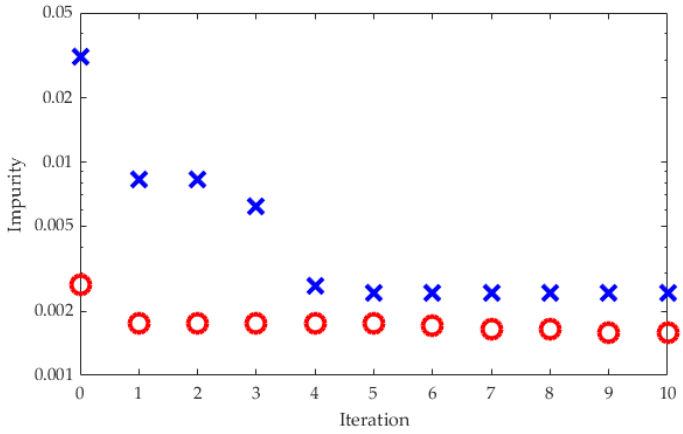

Figure 5.5: Optimizing the impurity for 10 iterations, displayed on a semi-log scale. The red circles is for a polarization where extinction is already good, while the blue crosses correspond to a polarization 90 degrees from the before mentioned.

The blue crosses correspond to a QD polarization where the phase front couples really well to the waveguide mode thereby creating a large background for the QD emission. Such a scenario is typically encountered when a specific QD dipole has to be excited with a specific well-defined polarization (e.g. for high efficiency QD single-photon sources or for spin experiments). Typically, optimally coupling to this dipole could lead to excess unwanted background. The technique discussed here can alleviate this limitation.

With the current algorithm that only optimizes beam deformations, we appear to be limited to an impurity of ~ 0.001. It would be interesting to investigate if there exists a fundamental limit on the best achievable impurity and the physical factors that determine this limits.

From Equation (3.29) ($g^2(0) \sim 2\xi - \xi^2$) it is known that there is a direct relation between the impurity and the second-order coherence. A test of the improvement is done by sending in pulsed laser and loading the optimization pattern on to the SLM.

Second-order coherence measured at π-pulse can be seen in Figure 5.6a, where counts have been normalized to a peak far away. The improvement is clear. Black is with no alterations to the wavefront and blue is phase corrected. Figure 5.6a represents the situation where a large fraction of the incident polarization scatter into the waveguide (blue crosses in Figure 5.5). In Table 5.1 the impurity together with the second-order coherence is shown. The relative improvement on impurity corresponds to a factor of 4 while the relative improvement on $g^2(0)$ is a factor of 3.

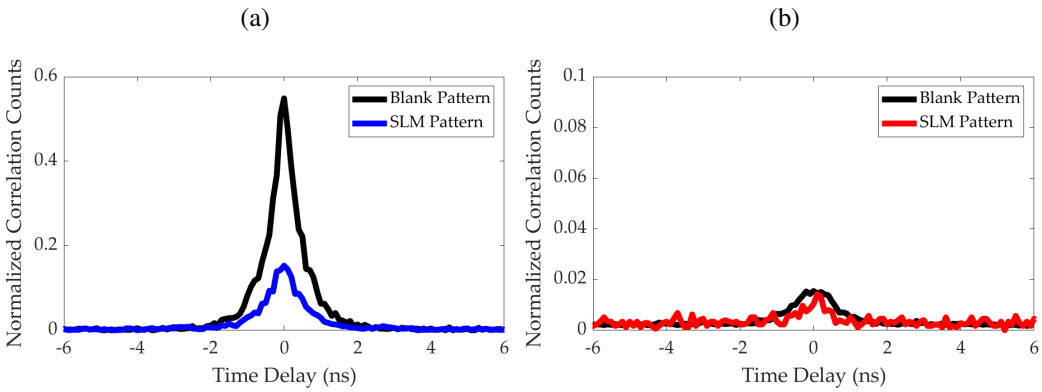

Figure 5.6: Second-order coherence measurement with (blue/red) and without (black) optimizing the phase of the wavefront using the SLM. The y-axis is normalized to a peak far away. $g^2(0)$ is measured at π-pulse. (a) is for a polarization where the laser is well-coupled to the waveguide mode. (b) is for the polarization where the impurity is already optimally suppressed.

Measurement	Impurity	$g^2(0)$
Ordinary Wavefront	0.23 ± 0.01	0.34 ± 0.03
Phase Correction	0.060 ± 0.008	0.11 ± 0.01

Table 5.1: Results on impurity and second-order coherence for a non-corrected wavefront and the SLM optimized wavefront. This corresponds to Figure 5.6a, where polarization is well-coupled to the waveguide mode. Uncertainty on impurity is calculated as standard deviation and for $g^2(0)$ error propagation is employed assuming Poisson-distributed noise in photocounting.

In case of optimal polarization for impurity, the results of improving impurity with the SLM can be seen in Figure 5.6b and Table 5.2. We saw from Figure 5.5 that the impurity has improved by a factor of 2. From Equation (3.29) we expect this to result in an improvement of the $g^2(0)$ just below a factor of 2. From the $g^2(0)$ measurements we do see an improvement, however due to short integration time the center peak is very small which makes it difficult to get a good estimate. The errors are therefore large and we might overestimate the actual $g^2(0)$. This measurement would improve by longer integration time. However, one should monitor the impurity while doing so. More on that in the next section.

Measurement	Impurity	$g^2(0)$	V_{raw}
Ordinary WaveFront	0.014 ± 0.004	0.019 ± 0.012	$0.83 \pm 0.05^*$
Phase Correction	0.0065 ± 0.0007	$0.007 \pm 0.003^*$	$0.87 \pm 0.05^*$

Table 5.2: Results for improvement of impurity, second-order coherence and raw indistinguishability with and without phase correction. This corresponds to Figure 5.6b, where polarization is optimized for lowest impurity. So the results are already quite good even without phase correction. * signifies that because of low counts, the estimate is not made by fit but by integrating the area under the peak. Errors on impurity are calculated from the fits and for $g^2(0)$ and V_{raw} errors are calculated by error propagation by assuming Poisson-distributed noise.

Doing a HOM measurement gives the results in the last column. The large errors are a result of low counts. The data can be seen in Figure 5.7. (a) is without wavefront correction

and (b) is with the SLM pattern. As seen the two look very similar. The dip is due to a large amount of dephasing on the QD. Fitting turned out to be difficult because of low counts and dephasing and overestimated the indistinguishability. A better estimate would be possible by fitting a bi-exponential to the center peak.

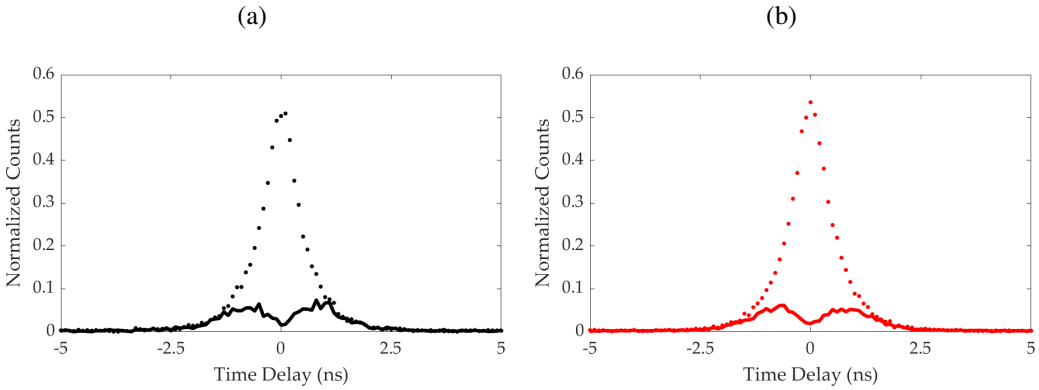

Figure 5.7: HOM measurements of the QD. The dots are the cross-polarized configuration, and the solid lines are the co-polarized configuration. Clear dephasing is observed. (a) Without the SLM pattern. (b) With the SLM pattern.

5.4 Stability Correction

From the results we see a clear improvement in impurity when phase correcting.

In Chapter 3 it was discussed how the setup suffers from free space optics, resulting in impurity decreasing over time. Figure 5.8 is reprinted here for convenience. As seen the impurity worsens with time and then retraces the relaxation over several hours to reach back to a minimum, making up a large triangle. The large triangle could for example be a mirror relaxing over time and this could be corrected by implementing a feedback loop that regularly (every 20 minutes) measures the impurity and corrects for such shifts by adding a phase.

A suggestion would be to already have an optimized stationary pattern on the SLM as has been shown here and then on top of that create an algorithm which checks the impurity by a quick 2 second measurement and if the impurity is off it will add another pattern, gradually shifting the overall phase as needed.

If considering employing this technique for conducting hands-free long time measurements one should be aware of possible phase jitter from the SLM. The amount of phase jitter for the current SLM should be reasonable low ($< 2\%$) so its effect should be negligibly small, however it should be checked as the pattern might need to be updated regularly for efficiency to be maintained.

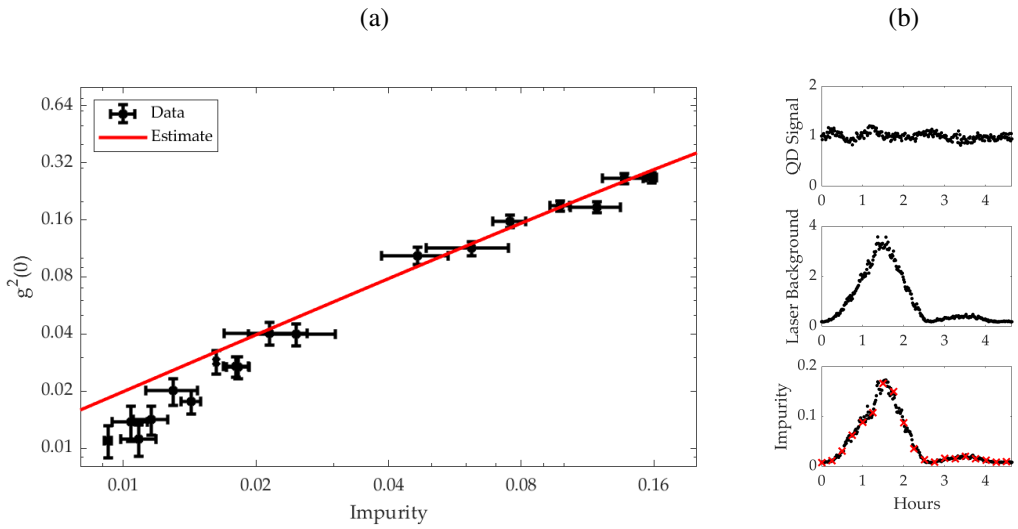

Figure 5.8: (a) Data are from one long measurement of second-order coherence, where the $g^2(0)$ worsens as impurity increases. Note the log-log scale. $g^2(0)$ is measured at pulse area π. The importance of impurity is clear. (b) Monitoring counts and background doing the long $g^2(0)$. The top panel shows the QD signal (normalized to the mean) being constant and only showing slow minor variations of 7%. The middle panel shows the laser background. The prominent triangle is suggested to be due to free optics straining and relaxing over more than 2.5 hours. It is clear that the scattering is causing the rise in impurity as seen in the bottom panel. The red crosses marks the interval from where the $g^2(0)$ measurements in (a) are made.

5.5 Summary

We have seen how the polarization of the excitation laser should not be exactly aligned to the orientation of the desired dipole as too much power would be needed to reach π-pulse which results in higher impurity of the collected emission. Therefore one should optimize for impurity (while still keeping counts reasonable) and choose a polarization that couples a small amount to the out-of-plane mode. This limits the source efficiency as a fraction of the undesired dipole is being excited.

To detect enough counts one may have to use a polarization where impurity is not at its lowest. However, it has been shown how scattering can be further suppressed by phase modification of the wavefront.

We have shown that by using a SLM to correct the phase of the wavefront, we can optimize for the least amount of scattering in collection by using a machine learning algorithm. By doing so, we see a direct improvement in the $g^2(0)$ as scattering from the pulse laser is the main contributor to impurity.

The improvement is clear for different polarization and so adding a phase correction should improve the operability of more polarization sensitive protocols.

It has been discussed how a natural next step would be to implement a feedback loop that for every few minutes correct the impurity by adding an overall phase making the setup hands-free for long periods of time.

CHAPTER 6

Pulse Length Dependence

From studies it is known that the pulse width of the excitation laser effects the second-order coherence of single photon emission [30][31]. The excitation process of the emitter is not in reality an instantaneous mechanism, the laser will always have some non-zero pulse length which imposes a fundamental limit to a perfectly pure single-photon source. This mechanism can be understood by studying the dynamics of multi-photon emission for longer pulse duration. The effect of excess laser scattering will be discussed in the short pulse regime. Furthermore, the relation between $g^2(0)$ and visibility will be studied in this chapter.

6.1 Pulse Length Dependence on Purity

By sending the excitation laser through a pulse stretcher, we control the pulse duration. Second-order coherence measurements have then been conducted.

The result of this can be seen in Figure 6.1. A X^0 QD with lifetime 650 ps has been resonantly excited and the photon emission has been filtered using a 3 GHz bandwidth spectral filter (combination of an etalon and a grating filter). $g^2(0)$ has been calculated using the data analysis method described in Chapter 3.

From the data we observe that the measurement of highest purity is $g^2(0) = 0.0086 \pm 0.0013$ measured at 12.3 ps. For longer pulses the $g^2(0)$ increases dramatically, and for shorter pulses the $g^2(0)$ stagnates or slightly increases. In the following sections, we will discuss the physical processes governing the observed pulse length dependence of $g^2(0)$.

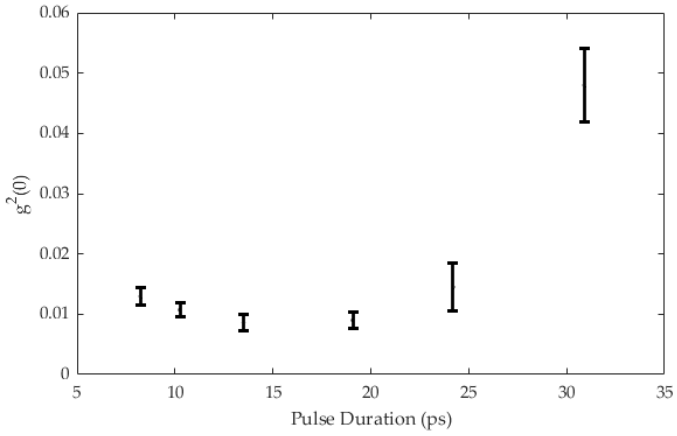

Figure 6.1: $g^2(0)$ for different pulse duration. The errors are calculated as statistical errors and vary due to different integration time.

6.1.1 Experimental Method

This section serves to break down the experiment.

Pulse Stretcher

For full control of the pulse duration the laser is sent through a pulse stretcher setup which stretches the pulse in time, while compressing it in frequency bandwidth.

The pulses from the MIRA laser has a duration of 4 ps and serves at the laser input. The available pulse stretcher setup is accomplished by sending the input laser through a beam expander and then onto a grating which separates the different frequency components of the pulse and reflects them in different angles. The light is then concentrated using a lens before being reflected by a mirror sitting in a mechanical slit. The light is sent back through the grating again, now with a π-phase shift from the reflection of the mirror making it possible to separate now stretched pulses from the laser input using a beam splitter.

The slit is small enough to clip the frequency bandwidth and by so only allow a part of the frequencies to be reflected, which is how the pulse is stretched. The slit width is adjustable by using a micrometer screw down to an order of 10 μm, which is what allow us to fine-tune the pulse width.

Calibration

To convert between slit width and actual pulse duration of the laser a calibration has been made and can be seen in Figure 6.2. The calibration is done by sending the output from the pulse stretcher onto a spectrometer. The lineshape of the laser is Gaussian, so by fitting to the spectra the FWHM can be extracted.

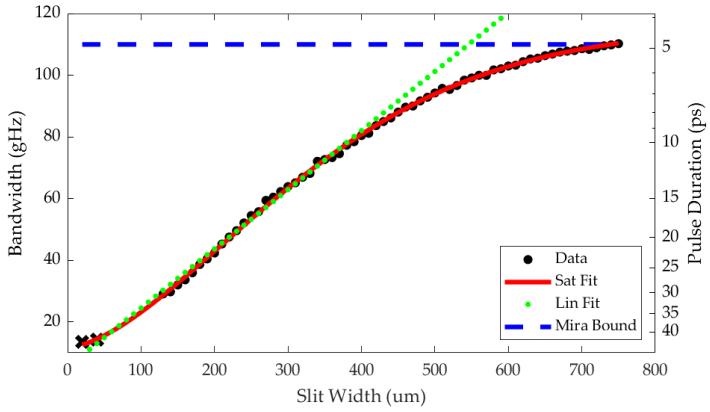

Figure 6.2: Calibrating the position of the slit to pulse width in GHz and pulse duration in ps. Data points are the FWHM extracted from Gaussian fits of the spectra of the laser. The first two points (crosses) are from voltage scans. Errors are within the marker size. The red line is the saturation fit, the dotted green line is a linear fit, while the dotted blue line is the unperturbed Mira laser.

The FWHM is then converted from bandwidth $\Delta\lambda$ to pulse duration $\Delta\tau$ using:

$$\Delta\tau = \frac{tbp \cdot \lambda^2}{c \cdot \Delta\lambda} \tag{6.1}$$

where by assuming a gaussian shape the time-bandwidth product is $tbp = 0.44$ and $\lambda = 947nm$ is the center wavelength.

The resolution of the spectrometer only allows for the FWHM to be reliably determined down to $\sim$ 30 GHz. Therefore, the first two points (crosses) are extracted from voltage scans of the QD emission at the specific slit width.

The curve starts to saturate around 4 ps, which is also the pulse duration of the laser (shown as the Mira Bound in Figure 6.2).

A saturation curve has been used as a fit:

$$f_{sat}(x) = a \cdot (1 - e^{-(x/P_{sat})^b}) + c \tag{6.2}$$

The data have also been fitted with a linear model, as we expect the mechanical slit to respond linearly. We see how the linear and saturation fit compares well until around 10 ps. By changing the slit width we can vary the pulse duration in a window between 4 to 40 ps spanning a window of 13-110 in GHz. One should be aware that for very long pulses the slit is just about open which could possibly create some single-slit interference.

Data Series

For different pulse width a series of power/impurity, second-order coherence, and HOM measurements have been performed. From the power series π-pulse is calculated so that $g^2(0)$ and HOM are both measured at π-pulse.

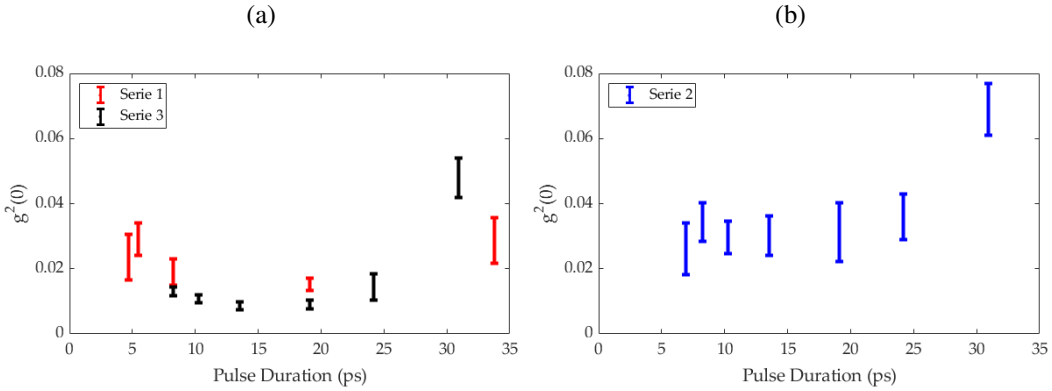

Figure 6.3: Data series of $g^2(0)$ for different pulse duration. (a) Series 1 and 3 are performed on the same quantum dot. (b) Serie 2 is performed on another QD but shows similar tendency.

As seen in Figure 6.3 the experiment has been performed several times resulting in three data sets, where only one of these (serie 3) were presented in Figure 6.1. Differences between the three series is as follows: The first series is on a dipole with lifetime 350 ps of a X^0 QD and for a long range but with fewer data points. The third series has been made on the second dipole of the QD where the lifetime was 650 ps. The second series has been made on a different X^0 QD, where impurity was slightly worse. A similar tendency of the $g^2(0)$ to increase with increasing pulse duration is consistent across the three series. This behaviour can be explained by multi-photon emission in the long pulse duration regime and will be discussed in the following section.

6.1.2 Multi-Photon Emission

If the single photon emission process is fast compared to a long laser pulse, then there is a probability that the QD returns to the ground state before the end of the laser pulse and is then re-excited. This leads to multi-photon emission. However, when the pulse duration is short compared to the spontaneous emission of the QD then re-excitation becomes unlikely.

Research has been done to study these mechanisms and establish a theoretical framework [30]. They are able to model $g^2(0)$ for different laser duration by providing analytic

approximations to the photon emission dynamics of a two-level system [32]. Using their results we can model $g^2(0)$. It is assumed that the probability for the source to emit more than two photons is negligible making: $g^2(0) \approx \frac{2P_2}{(P_1+2P_2)^2}$, where P_n is the probability for n photon emission. This has been attempted in Figure 6.4c. The $g^2(0)$ is clearly getting worse for longer pulse duration. Which is consistent with the experimental results from Figure 6.1.

This dependence can be intuitively understood by considering re-excitation dynamics. The excitation pulse is not infinitesimally short, but has some certain duration, so it must be considered how the system evolves during the excitation interaction.

Figure 6.4a explains the presence of a pulse interacting with the system. The black line shows the system being driven to the excited state (where $P_e = 1$) as the system absorbs the laser pulse completely. After the pulse has ended the system will decay spontaneously at some later time. This is the ideal single-photon source. Exactly one photon is emitted when the source is being probed. The dotted red line shows one photon being emitted during the interaction, after only absorbing half of the excitation pulse. After spontaneous emission the system collapses to the ground state and the Rabi oscillations then restarts and re-excites the system. Which ends up in some superposition state where it might emit a second photon at a later time. This is re-excitation and is the phenomenon causing our single-photon source deviates from the ideal case.

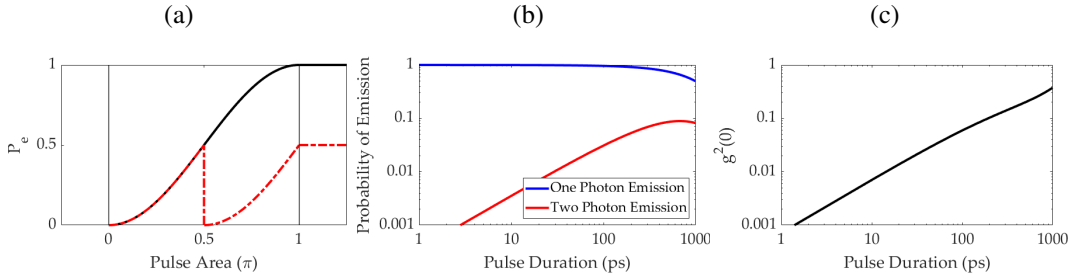

Figure 6.4: Re-excitation dynamics of TLS interacting with π-pulse (a) Scheme of system-pulse interaction when (solid black line) no photon is being emitted doing the pulse and (dashed red line) one photon is emitted and re-excited within the pulse-window. (b) Simple model of the probability of (blue) one photon (red) two photon emission (P_1 and P_2) as a function of laser pulse duration. Notice semi-log scale. (c) Simple model estimating $g^{(2)}(0)$ as a function of laser pulse duration, this is based on numbers from (b).

Most of the time we expect the TLS to behave ideally and only emit one photon at a time (for π-pulse), but if the pulse-window is large compared to the lifetime of the QD then the system has more time to re-excite. That is, it becomes more likely that two photons will be emitted doing one laser pulse. This is seen in Figure 6.4b, where expressions from [30] has been used to model the emission. The only variable in their model being the spontaneous emission rate of the QD, which has been set to 2.78 ns^{-1} equivalent to a lifetime of 350 ps. Notice the semi-log scale.

It should also be noted that this model is believed to be accurate up to 100 ps [30], which is well within the window that we are working in.

6.1.3 Short Pulse Duration

Now moving away from the long pulse regime we consider the effect that shorter pulses has on $g^2(0)$. From the model above it is implied that $g^2(0)$ should continuously improve for shorter pulses [30]. However, from the results in Figure 6.1 this does not necessarily seem to be the case. Here we notice that $g^2(0)$ is a little larger for very short pulses < 10 ps. A reason for this could be found by studying the power and impurity dependence on pulse duration.

6.1.4 Pulse Length Dependence on Impurity

For each pulse width a serie of power measurements is run to calculate the power to reach π and the impurity by the method described in Chapter 3. Figure 6.5a shows power at pulse area π plotted as a function of pulse duration. The blue markers are measurements done with the use of a 3 GHz etalon and a 22 GHz grating filter. The red markers are for the unfiltered emission. Filtering is done in order to prevent emission from other QDs (further discussion in the next section).

We see how the filtered and unfiltered data both follow the same curve which indicates that if there is another QD being excited the relative emission from it is not very pronounced.

The power dependence at π-pulse can be described by considering that the Rabi frequency Ω is proportional to the peak power P.

$$\Omega \propto \sqrt{P}T \tag{6.3}$$

For π-pulse the Rabi frequency is constant, which means that:

$$P \propto \frac{1}{T^2} \tag{6.4}$$

But as we are actually measuring the average power and not the peak power we find that:

$$\langle P \rangle_{avg} \propto \frac{P}{T} \tag{6.5}$$

So we expect the data to follow a power function $\langle P \rangle_{avg} = a \cdot T^b$ with $b = -1$. We estimate $b = -0.96$ by fitting the filtered data.

In Figure 6.5b The impurity is measured for the same data as shown in (a). We observe how the filter consistently reduces the laser background for every pulse duration of the excitation laser.

In Figure 6.5c power vs impurity from (a) and (b) are plotted. It is clear that the impurity increases linearly in the unfiltered case, while it is strongly suppressed for the filtered data.

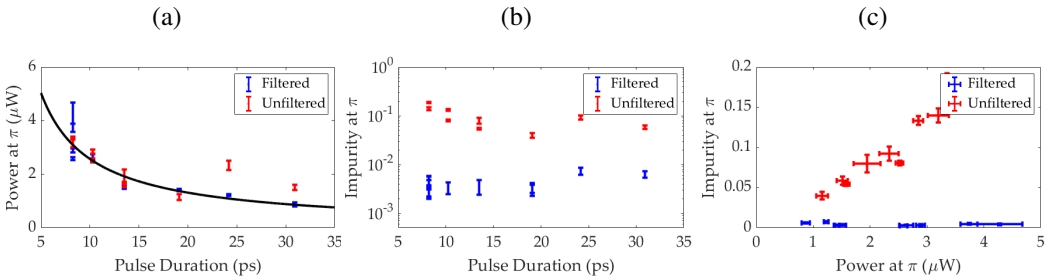

Figure 6.5: Pulse dependent measurements (a) Power at π for different pulse duration for unfiltered and filtered emission. Filtered emission is fitted with a power function. (b) Impurity at π for different pulse duration for unfiltered and filtered emission. Note the semi-log scale. (c) Comparison between data in (a) and (b).

So, it is observed how the power needed to reach π-pulse increases as the bandwidth increases. This can be understood by considering how the wider bandwidth of the laser results in more spectral components away from the QD transition and therefore a smaller overlap between the system transition and incoming pulses, which results in more laser power needed to excite the QD at π-pulse. More power going onto the sample is inevitably going to create more scatter increasing leakage into the detectors.

Furthermore, it is shown that ultrashort pulses because of their broad bandwidth more easily interacts with random media and the scattering thereof becomes larger with larger variations [33], which could in principle create more scatter in the system.

As has been discussed in Chapter 3 we know that the impurity is highly dependent on the laser background in the system, which linearly increases with power. This is seen in Figure 6.5c.

Our measurements confirm that for this short pulse duration the main contribution to $g^2(0)$ stems from imperfect laser suppression.

This suggests that there is a limit to how short pulses should be for realizing optimal single-photon sources. One should balance the dynamics of re-excitation for long pulses with the detrimental effects of broad frequency for short pulses.

This work suggests that the preferred pulse width is around $\tau_{laser}/\tau_0 \sim 0.06$, where τ_0 is lifetime of the QD and τ_{laser} is pulse duration of the excitation laser.

6.2 Effect of Spectral Filtration

A high density of QDs on the sample means that when exciting from the top one might excite other QDs within the size of the laser beam. Therefore a filtration system of using two spectral filters for the photon emission has been applied. The two spectral filters are a 3 GHz etalon and a 22 GHz grating filter.

From Figure 6.5b it is seen how the scattering is consistently being suppressed by using filters, causing the impurity to stay constant for increasing power.

Figure 6.6 shows the effect that adding a filter has on the second-order coherence as well as for raw HOM visibility.

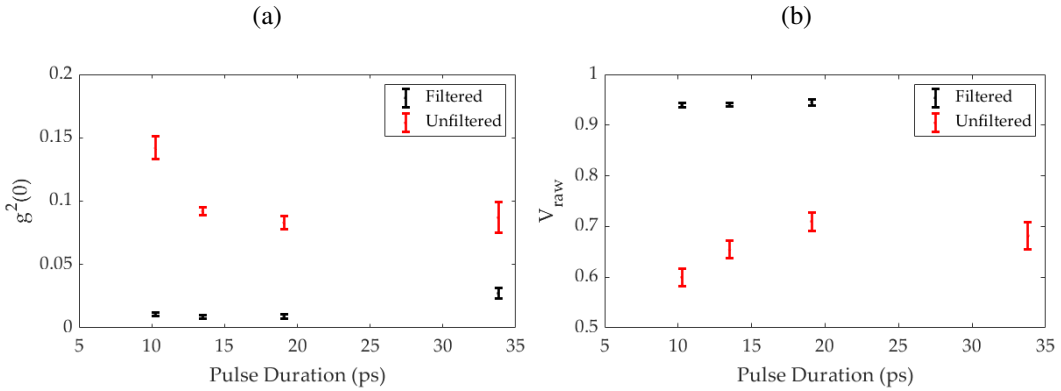

Figure 6.6: Effect of filtering on measurements (a) Filtered and unfiltered second-order coherence measurements at π-pulse. (b) Filtered and unfiltered visibility measurements at π-pulse.

6.3 Pulse Length Dependence on Indistinguishability

Hong-Ou-Mandel measurements for different pulse duration have also been performed. The result of this can be seen in Figure 6.7 for the three series, where the visibility has been corrected for beam splitter asymmetry and classical interferometer error. The indistinguishability exhibit only slight changes across different pulse duration. The best achieved visibility is $96 \pm 1\%$, without correcting for the non-zero $g^2(0)$.

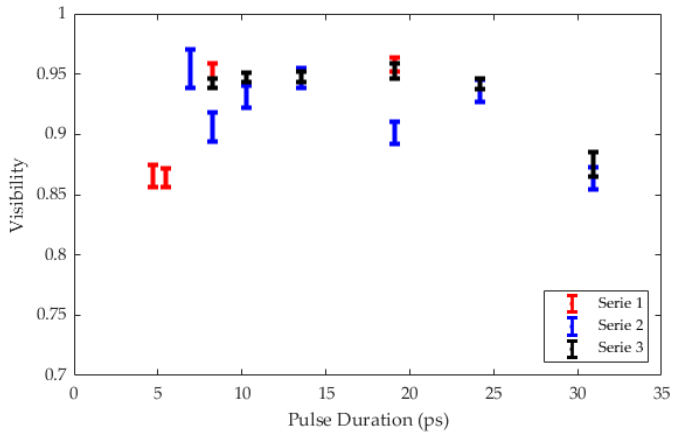

Figure 6.7: Visibility calculated from HOM measurements at π-pulse for different pulse duration. The three series are the same three runs described in the previous section.

It seems that the indistinguishability is not directly dependent on the pulse duration of the excitation laser. However, it is still indirectly through the non-zero $g^2(0)$ as can be seen in Figure 6.8, where corresponding pairs of $g^2(0)$ measurements and intrinsic visibility has been plotted. These measurements are from the third dataserie.

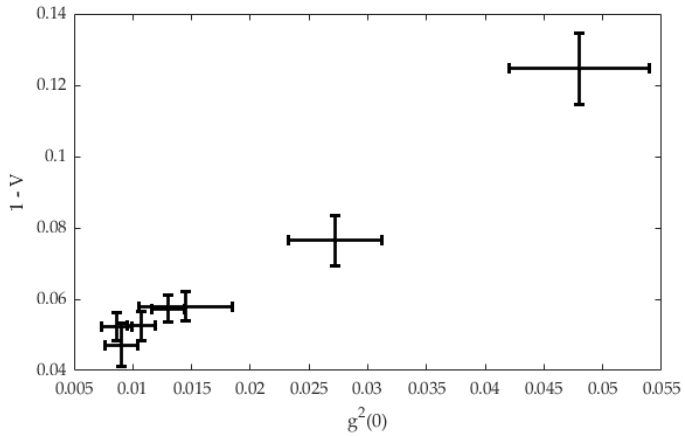

Figure 6.8: Shows the relationship between $1 - V$ and $g^2(0)$ for the third dataserie.

From this figure it is clear that an imperfectly pure source will effect the indistinguishability of the emitted single-photon pulse train from the QD. The dependence seem to be linear, however an exact relation is not easily determined as will be made clear in the following section.

6.4 Non-zero $g^2(0)$ Correction to Visibility

In Chapter 3 we showed that the visibility calculated from a HOM measurement is directly equal to the single photon indistinguishability $|\langle f_i|f_j\rangle|^2$:

$$V = |\langle f_i|f_j\rangle|^2 \equiv M_S \tag{6.6}$$

By correcting for the beam splitter asymmetry and the classical interference error we are able to estimate visibility from HOM measurements. However, visibility is also dependent on a non-zero $g^2(0)$ as shown above. So, a intrinsic estimate, V_{int}, would require a correction of the $g^2(0)$, which is also often how visibility is presented in literature [20][11].

Assuming separable noise and a small $g^2(0)$ then the visibility becomes [31]:

$$V_{int} = M_S - \left(\frac{1+M_S}{1+M_{SN}}\right) g^2(0) \tag{6.7}$$

Where M_{SN} is the wavepacket overlap between additional 'noise' and the single photons, satisfying: $0 \leq M_{SN} \leq M_S$

For $g^2(0) = 0$ the equation is as before.

To understand this equation better it is beneficial to consider the two limiting cases:

If the additional photons are identical to the single photons, that is $M_{SN} = M_S$, then:

$$V(M_{SN} = M_S) = M_S - g^2(0) \tag{6.8}$$

resulting in a line with a slope of negative 1 on a visibility vs $g^2(0)$ plot.

Alternatively in the limit where the noise is distinguishable from the single photons: $M_{SN} = 0$ the equation becomes:

$$V(M_{SN} = 0) = M_S - (1+M_S)g^2(0) \tag{6.9}$$

a line with a slope between negative 1 and 2 depending on M_S.

From this it becomes clear that the dependence between the intrinsic visibility and a non-zero $g^2(0)$ relies on the origin of the 'noise' photons, that is how indistinguishable/distinguishable they are.

Tracking the origin of noise is no simple task. An approach would be to assume that the noise consists of contributions form two different sources [31] that being: 1) re-excitation and 2) imperfect suppression of the excitation laser.

A re-excitation process would result in the 'noise' being close to (but probably not perfectly) indistinguishable from the single photons, which would tend towards the limit $M_{SN} = M_S$. While background laser scattering would create much more distinguishable noise resulting in the other limit $M_{SN} = 0$.

Figure 6.9 displays the visibility vs $g^2(0)$, where the grey area is restricted between the two hard limits. The data points are the consecutive measurements of $g^2(0)$ and visibility also presented in Figure 6.8. A linear fit shows that the measurements fall somewhere in between the two limits with a slope of $M_s = -1.8$. This indicates that the noise in our QD consists of a combination of indistinguishable and distinguishable noise.

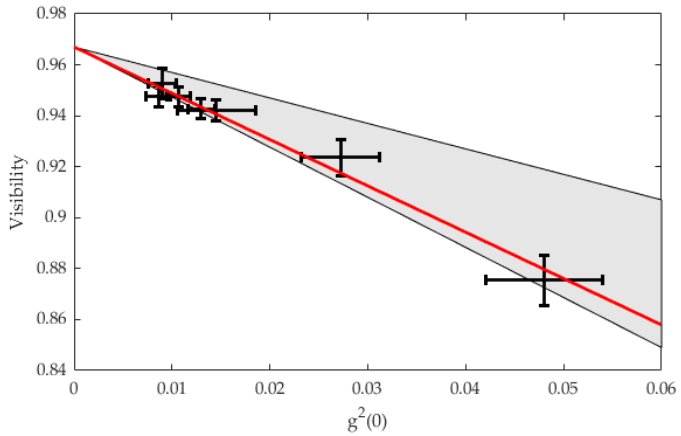

Figure 6.9: Raw visibility vs $g^2(0)$ plot for filtered data. The red line is a linear fit while the grey area confines the limiting values of the simple model discussed above.

That is, the data show signs of both re-excitation and laser scattering. However, to experimentally determine the exact origin and the quantity of the excess noise is yet to be investigated.

It should also be noted that decreasing the pulse duration might introduce additional distinguishable noise, so it is not certain that each point in Figure 6.9 should be on the same linear slope. However, that they do fall within the grey area is a good indication that changing the pulse width might not change the noise origin too much, so this consideration might only be significant when spanning a wider range of pulses.

While the exact mathematical relation between visibility and $g^2(0)$ can be argued upon, it is clear that there is a direct impact on visibility by $g^2(0)$.

The lowest $g^2(0)$ is at pulse duration 22 ps with a $g^2(0) = 0.0086 \pm 0.0013$ this is also where the best indistinguishability is measured at: $V = 96 \pm 1\%$

6.5 Summary

Figure 6.1 is the main result of this chapter. The $g^2(0)$ depends on the pulse duration of the excitation laser. We have discussed how the ability of a laser pulse to drive re-excitation in a two-level system places a fundamental limit to the emitter behaving as a single-photon source for long pulse duration. While for shorter pulse duration a higher power at π-pulse creates more scattering in the system which might limit the purity. Furthermore it is clear from the empirical data that a non-zero $g^2(0)$ directly impacts the indistinguishability as shown in Figure 6.9. The field would benefit from exact theoretical modelling of such as well as experimental investigation into the origin of noise.

An interesting investigation for further research would be to explore different pulse shapes while optimizing for more efficient and higher-purity single photon emission.

CHAPTER 7

Two-Photon Excitation Scheme

Different excitation schemes can be applied to optically excite the QD and generate single photons. The work presented so far has been with the resonant excitation (RE) technique of which the advantages and disadvantages will be further discussed in this chapter. Lately, interest have gone into using an alternative excitation scheme for single photon generation using two-photon excitation (TPE) of the biexciton state [34][35][36]. Work on this protocol will be presented in the second part of this chapter.

7.1 Resonant Excitation

With the resonant excitation technique the excitation laser is resonant with the QD transition. This has the advantages of completely eliminating excitation timing jitter, since the excitation laser and the emission have the same energy, so no additional carriers or photons are generated that may cause undesirable dephasing processes.

A clear challenge is imperfect filtering of the laser background. A common approach is to use cross-polarized detection, or through weakly coupled optical modes (e.g. out-of-plane illumination of a QD coupled to a photonic crystal waveguide as employed in this thesis).

While cross-polarized excitation-collection geometry has been commonly used, this scheme comes with the disadvantage of a theoretical upper limit of 50% collection efficiency. Photonic crystal waveguides have gained from investigations over the past years, where the generation of pure single photons with high indistinguishability has been demonstrated [1]. In recent work using photonic crystal waveguides, we present the realization of a deterministic single-photon source featuring near-unity indistinguishability with an intrinsic visibility of $96 \pm 2\%$ and purity of $g^2(0) = 0.015 \pm 0.005$ achieved using resonant excitation [11]. In that paper it is furthermore reported how the source has a total generation rate of 122 million photons per second.

These measurements were conducted at π-pulse where the rate of generation is the highest. However, studies have suggested that the $g^2(0)$ might improve for pulse areas below π-pulse [30].

As has already been discussed in earlier chapters the $g^2(0)$ doing resonant excitation is limited by non-zero impurity due to imperfect suppression of the laser scattering as well as re-excitation.

7.2 Two-Photon Excitation

For resonant excitation the two-level system consisting of the exciton $|X\rangle$ and ground state $|g\rangle$ of a QD is the transition being addressed.

Instead, we can consider a four-level system consisting of the biexciton $|XX\rangle$, two excitons $|X\rangle$, and the ground state $|g\rangle$, see Figure 7.1.

The biexciton is as the name suggests the second creation of two electron-hole pairs. Due to the asymmetry of the QD the two exciton levels have slightly different energies resulting in the fine structure splitting Δ.

In this scheme a two-photon excitation (TPE) process initially prepares the system in the $|XX\rangle$ [37]. Due to the Coulomb interaction, the binding energy of the biexciton is lower than the exciton, which results in a spectrally non-degenerate photo emissions (one from $|XX\rangle \rightarrow |X\rangle$ and the other from $|X\rangle \rightarrow |g\rangle$). The laser is tuned to an energy corresponding to half the energy difference between $|g\rangle$ and $|XX\rangle$ and is therefore detuned from both the $|X\rangle$ and $|XX\rangle$ photoemission energies. The system then decays as $|XX\rangle \rightarrow |X\rangle \rightarrow |g\rangle$ via the cascaded emission of two photons. The biexciton state decays approximately twice as fast as the exciton state.

Single photons can then be obtained by frequency filtering either on the $|X\rangle$ or $|XX\rangle$ transition.

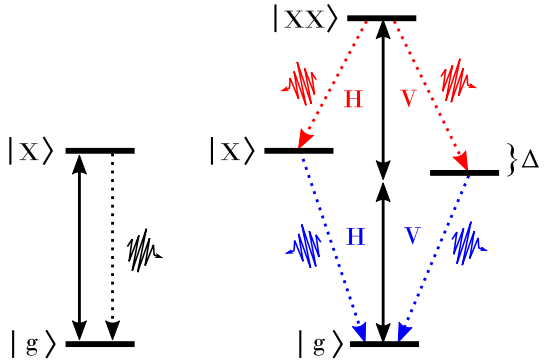

Figure 7.1: Energy diagrams for photon generation. Solid lines are the excitation laser, while dotted lines are the QD emission. To the left is resonant excitation scheme. To the right is the two-photon excitation scheme of the biexciton–exciton cascade, where the biexcition is resonantly excited by two laser photons.

Clear advantages of the TPE scheme include essentially background-free single photons as the excitaiton laser is detuned by around 1 nm from the QD transitions. On GaAs/AlGaAs quantum dots embedded in a low-Q planar cavity this has resulted in ultra pure single-photons with second-order coherence of $g^2(0) = (7.5 \pm 1.6) \cdot 10^{-5}$ [35]. A much better result than what has been achieved for resonant excitation.

Furthermore, as discussed in the previous chapter, the ability of a laser pulse to drive re-excitation in a TLS fundamentally limits purity of the generated photons. But a TPE scheme is much more robust to re-excitation as there is a ultra-low multiphoton probability [36].

With resonant excitation of the exciton state, re-excitation can directly occur after the initial emission of the single photon. But in TPE the laser is addressing the biexciton state which then decays to the exciton. Re-excitation can only occur once the system has returned to the ground state, which is delayed by the lifetime of the exciton state unless the energy detuning from the laser is sufficient to pump either of the intermediate channels. So by the time the system has completed its cascaded decay: $|XX\rangle \rightarrow |X\rangle \rightarrow |g\rangle$, and returned to the ground state, the intensity of the excitation laser pulse is much lower than it would be after only a single decay. Thereby suppressing re-excitation.

7.2.1 Experimental Realization of TPE

Two-photon excitation has been attempted on two different QDs as a consistency check. For QD1 the emission recorded on a spectrometer can be seen in Figure 7.2.

In the case of QD1 the laser is positioned at wavelength 948.2 nm which is 1 nm between the $|X\rangle$ and $|XX\rangle$, which are marked in blue and red respectively.

The noisy environment of the $|XX\rangle$ emission is due to other QDs being excited by the laser as well as laser scattering. When doing measurements the emission is filtered and because the energy of the excitation laser is detuned from the emission energies of both $|X\rangle$ and $|XX\rangle$ we can suppress the laser by spectral filtering. This is seen in the figure below where a grating filter is applied around the $|XX\rangle$. It is clear that the filtering process removes the unwanted emission pretty well.

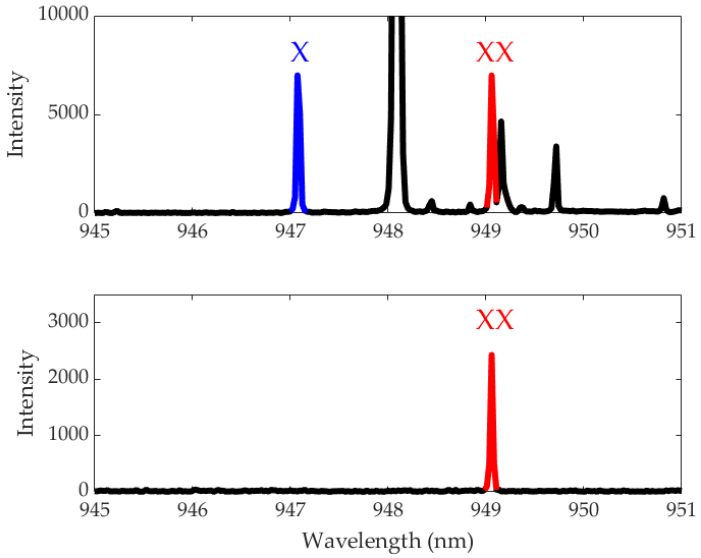

Figure 7.2: Spectrum for two-photon excitation. The laser is at 948.2 nm. The exciton $|X\rangle$ is at 947.3 nm and the biexciton $|XX\rangle$ is at 949.1 nm. From the upper plot it is clear that other QDs close to $|XX\rangle$ are being excited as well. The lower plot shows the emission when filters are applied. The intensity is in arbitrary units as these two measurements are done for different powers.

As seen in Figure 7.3 to reach π-pulse a power of 48 μW is needed because of the detuned laser, which is substantially more than that required for resonant excitation. Also from the emission spectrum it seemed as though the emission intensity was identical for $|X\rangle$ and $|XX\rangle$ which is also what would be expected in the ideal case since the emission of $|X\rangle$ is conditioned on the decay of $|XX\rangle$.

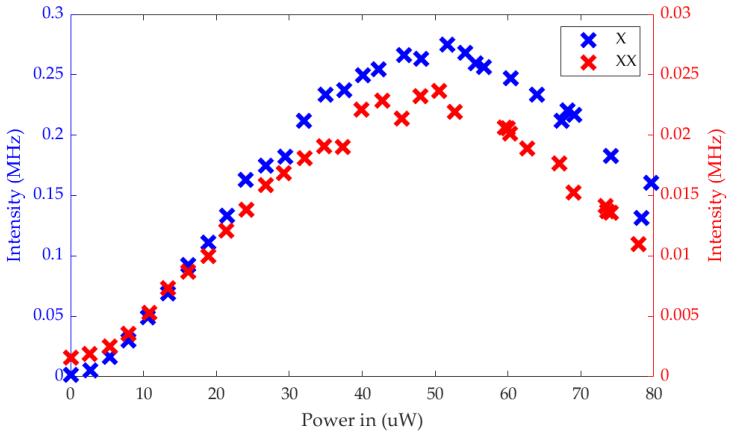

Figure 7.3: Powerseries of the TPE emission from QD1 when filtering around $|X\rangle$ (blue) and $|XX\rangle$ (red). π-pulse is at 48 uW. Note the intensity difference between the two states.

However, as seen in Figure 7.3 there is more than a factor 10 difference between the

two, with the $|XX\rangle$ being much lower.

This mismatch in intensity seem to be a filter efficiency issue due to the difference in efficiency of the two filtering setups used for the exciton and biexciton emission, as the exciton and biexciton peaks are equally intense on the spectrometer. QD1 is the quantum dot that was characterized in Chapter 2 as well as used for the pulse duration experiment in the preceding chapter. This QD had a fine structure splitting of ~ 6 GHz, so when collecting the $|X\rangle$ emission we need to use the etalon filter on top of the grating filter in order to filter away the second dipole. This of course lowers the efficiency.

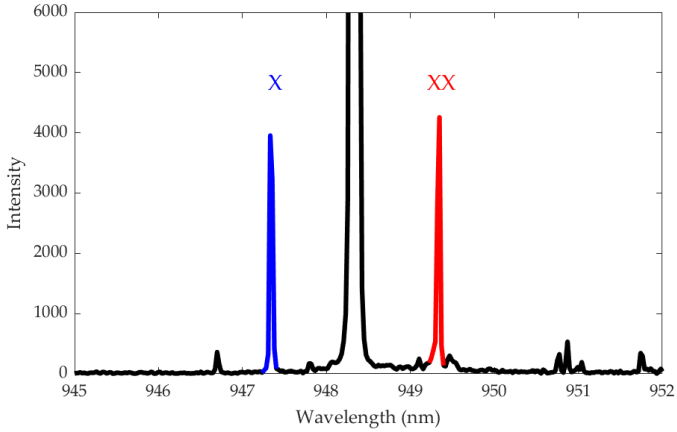

Figure 7.4: Spectrum for two-photon excitation for QD2. The laser is at 948.3 nm. The exciton $|X\rangle$ is at 947.4 nm and the biexciton $|XX\rangle$ is at 949.3 nm. The unfiltered emission is clean compared to QD1.

TPE has also been conducted on another QD (here onward named QD2) which had lower noise in the proximity of $|XX\rangle$ see Figure 7.4. QD2 had a much larger fine-structure splitting of ~ 10 GHz, which means that we only minimally excite the second dipole, and we therefore do not need to use the etalon filter for collecting the emission from $|X\rangle$ while doing TPE.

The powerseries for this QD (see Figure 7.5) shows that π-pulse is around $50\mu W$ similar to QD1, however the intensity mismatch between the two states is though still present much lower with only a factor of 2 between them. This indicates that the mismatch in efficiency between the two filtering setups has been reduced.

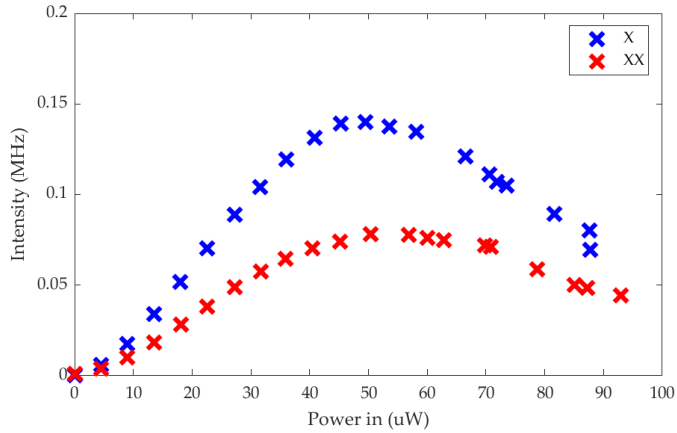

Figure 7.5: Powerseries of the TPE emission from QD2 when filtering around $|X\rangle$ (blue) and $|XX\rangle$ (red). π-pulse is at 50 uW.

Figure 7.6 shows the powerseries of the emission when resonantly exciting the exciton

of QD1. For single photon generation it is desirable to work at π-pulse for increasing the emission rate. π-pulse for resonant excitation is around $3\mu W$ while it was around $50\mu W$ for TPE. Doing TPE does require a setup that can handle that amount of power without introducing unwanted scattering. Also the collection efficiency is generally higher for RE as we could employ only a single etalon filter (efficiency $\sim 88\%$) in comparison to a grating filter (efficiency $\sim 40\%$) that was required for TPE in order to suppress unwanted emission and the laser. The impurity at π-pulse for RE is $\xi = 0.0078$. While for TPE the impurity is basically zero as any laser scattering is small enough to be hidden within the dark counts.

Second-order coherence measurements and HOM measurements has been conducted at π-pulse for both QD1 and QD2. The results are similar, and therefore only data from QD2 is presented here, see Figure 7.7.

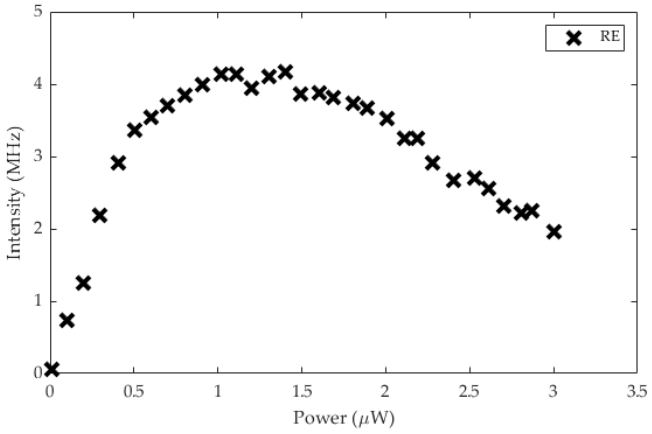

Figure 7.6: Powerseries of RE of exciton of QD1.

Figure 7.7 is the main figure for this chapter and compares second-order coherence and HOM measurements for RE of the exciton, and TPE for the exciton and biexciton.

The top panel shows resonant excitation. We extract $g^2(0) = 0.015 \pm 0.005$ and intrinsic visibility $96 \pm 2\%$. The additional dips in $g^2(0)$ are from detector noise. It should be noted that this is similar to what was achieved for QD1 before optimizing pulse duration. This shows the consistency of high quality QDs in the sample and QD2 could probably have lower $g^2(0)$ if more careful optimization was conducted.

For the middle panel we have the emission from $|X\rangle$ doing TPE, in the $g^2(0)$ there is an antidip at zero time delay where the counts go down below the background level. This can be explained by considering the cascade process where the exciton decay is conditioned on the biexciton decay. The dip is a clear indicator of the high purity of the $|X\rangle$ single photon emission.

For the $|XX\rangle$ there is a small peak at zero time delay which gives a $g^2(0) = 0.035 \pm 0.007$. This could be due to the biexciton being re-excited before decaying to the exciton state.

The visibility calculated from the HOM measurements of $|X\rangle$ and $|XX\rangle$ are both just below 60%. On $|X\rangle$ we see dephasing indicating that the second dipole is suppressed. This is similar to QD1 when using both filters. With only the grating filter QD1 has a visibility of $(\sim 35\%)$ for both $|X\rangle$ and $|XX\rangle$ doing TPE and no dephasing was present.

So even though TPE excel in pure single photon generation of the $|X\rangle$ the indistinguishability is not as impressive as the case is for resonant excitation.

The degree of indistinguishability of photons doing TPE has been investigated in [38]. They experimentally find a similar limit to the visibility of around 70% and suggest that it is connected to the lifetime of the transitions such that visibility is limited by:

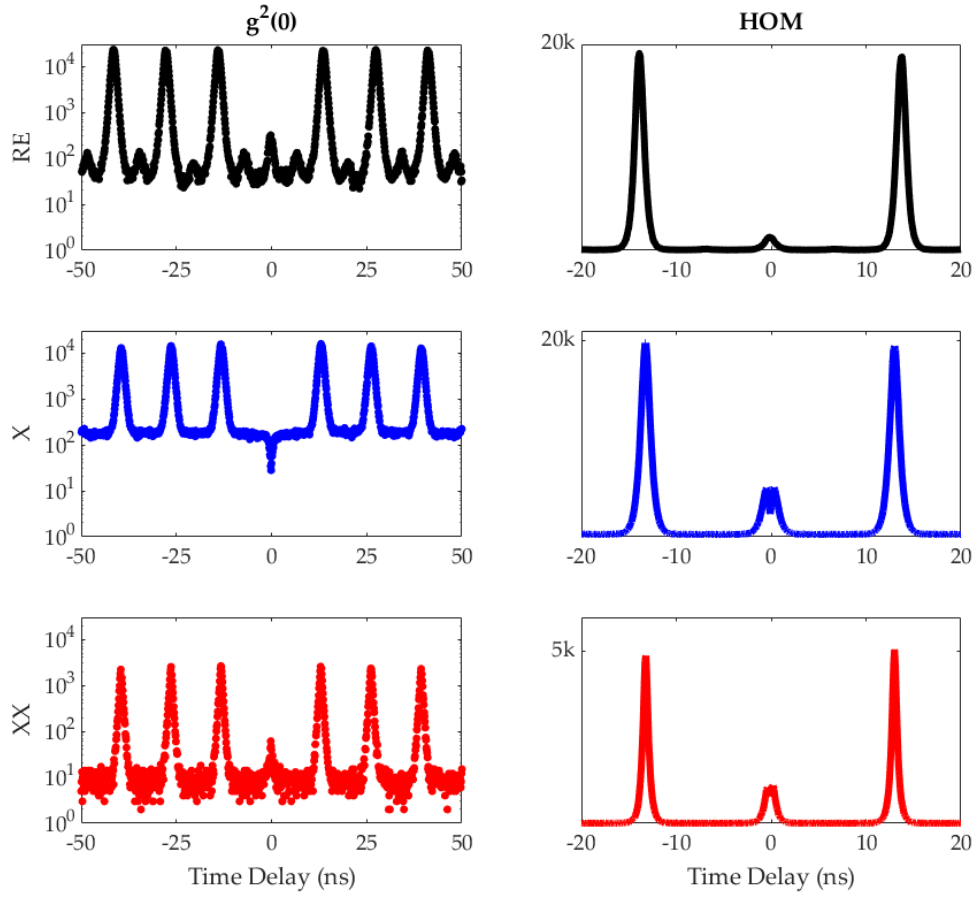

Figure 7.7: Second-order coherence measurements and Hong-Ou-Mandel measurements under resonant excitation (RE) and two-photon excitation for both the exciton $|X\rangle$ and biexciton $|XX\rangle$ performed at π-pulse on QD2.

$$V = \frac{\gamma_{XX}}{\gamma_{XX} + \gamma_X} \tag{7.1}$$

where $\gamma_{X(X)}$ is the decay rate of the (bi)exciton.

As mentioned the typical emission of the biexciton has around twice the rate of emission from the exciton: $\gamma_{XX} = 2\gamma_X$. Figure 7.8 shows a lifetime measurement for the exciton and biexciton emission. The decay rates were measured to be $\gamma_X = 2.10\text{ns}^{-1}$ and $\gamma_{XX} = 4.01\text{ns}^{-1}$ from the fits.

which makes the maximum achiebable visibility limited to $\sim 66\%$. This means that the visibility is dependent on the decay ratio. So that for small values of $\frac{\gamma_{XX}}{\gamma_X}$ the indistinguishability is almost zero and then increases to near unity for larger ratios. Therefore, to achieve high indistinguishability the limit where the biexciton decay is much faster than the exciton decay is desired. In that limit the system would essentially behave like a TLS where the exciton state is so very long-lived that it behaves as a ground state. Such a source could achieve the best from both the RE and TPE schemes.

This effect can be understood by considering the decay dynamics of the system. The photons emitted by the biexciton are spectrally broadened due to the linewidth of its short lived final state (the exciton) resulting from its non-zero decay rate. On the other hand photons emitted from the exciton does not broaden as their final state is an actual ground state, however the exciton is subjected to timing jitter induced by the cascade from the biexciton. Tuning the ratio of the decays might be experimentally realized by nanophotonic

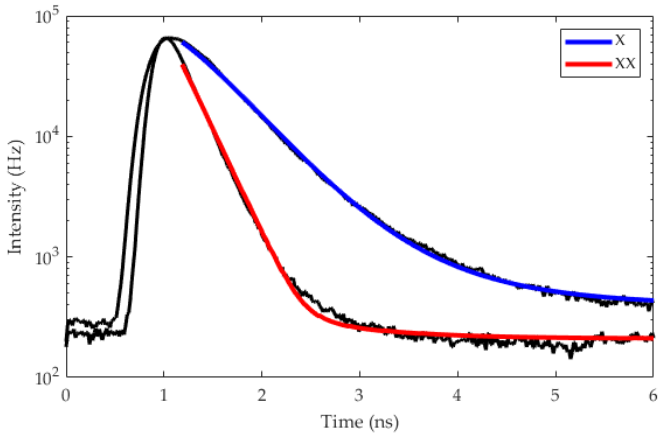

Figure 7.8: Lifetime measurement for $|X\rangle$ and $|XX\rangle$ under TPE for QD1.

structures that selectively enhances (reduces) the decay of γ_{XX} (γ_X). It should be noted that an asymmetric Purcell enhancement of both transitions is preferred over Purcell suppression to maintain efficient rate of photon generation.

7.2.2 Blinking

While it is desired that the quantum emitter behaves as an ideal four-level system when doing TPE, in reality it might possess a very complicated level structure.

Figure 7.9 shows the integrated coincidence counts from long timescale second-order coherence measurements up to $50\mu s$. The counts have been normalized to the peak area furthest away.

As can be seen in the top panel, under resonant excitation, only a small amount of bunching is present. This indicates that there is very little random blinking to dark states happening. However, a large amount of blinking is observed for both the exciton and biexciton under TPE. To study this behaviour further coincidence measurements has been performed for several different powers and the blinking has been fitted using an exponential function with an offset as can be seen in Figure 7.10 for both $|X\rangle$ and $|XX\rangle$. The blinking gets more pronounced for larger powers closer to π-pulse. And is a little worse for the $|XX\rangle$ as seen in Figure 7.11, where the decay rates of the fits have been extracted.

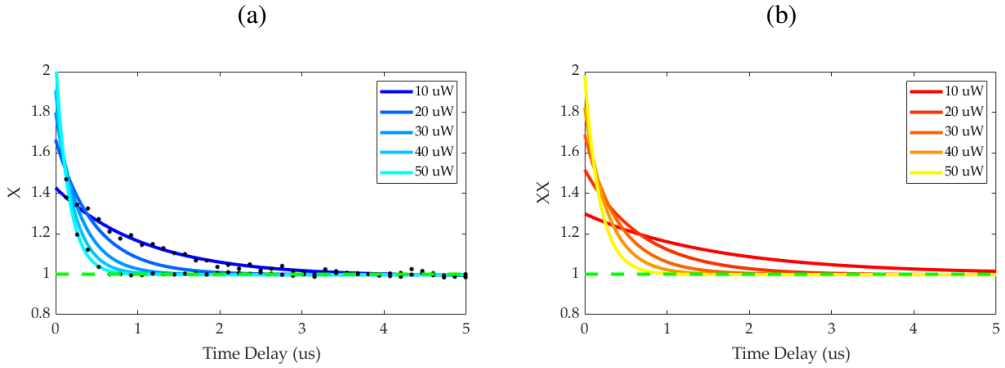

Figure 7.10: Exponential fits of the integrated counts for different laser powers for the exciton (a) and biexciton (b). The blinking is clearly power dependent. On (a) the black markers are the data points for which 10μW and 50μW has been fitted to. Only 1% of the points are shown for clarity's sake.

Power dependent blinking implies the presence of dark state [39]. Blinking comparable

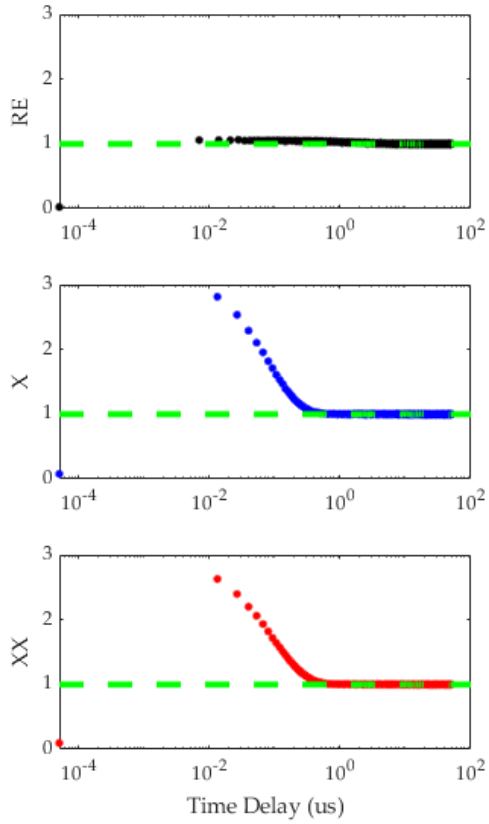

Figure 7.9: Integrated coincidence counts under each peak over a long timescale of $50\mu s$ and normalized to the area of the peak furthest away. For resonant excitation minimal blinking is observed. For TPE blinking is very present for both the exciton and biexciton.

to this was present for QD1 as well. The large amount of blinking does indicate that the system is behaving far from ideal, which is not a desired feature for realizing single-photon sources and could be the reason for the non-zero $g^2(0)$ measured for the $|XX\rangle$.

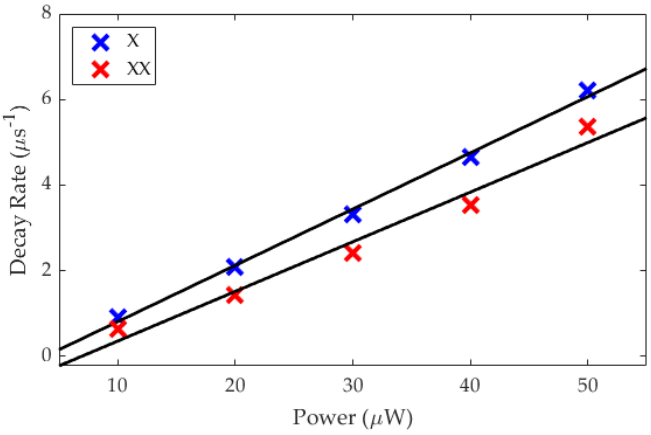

Figure 7.11: The power dependent decays extracted from the fits in Figure 7.10. The black lines are linear fits.

7.3 Summary

In summary, we have compared the resonant exciton of the TLS to the two-photon excitation (TPE) scheme of the biexciton cascade in search for an ultimate scheme for on-demand pure single photon generation.

Resonant excitation excels in indistinguishability with an intrinsic visibility of $V = 96 \pm 2\%$. However, due to re-excitation and imperfect supression of the laser scattering it does have an non-zero $g^2(0)$. TPE shows promising results in term of ultra pure photons due to the background-free technique and robustness to re-excitation. However, for the TPE the best visibility was measured to be 60%.

It has been discussed how a possible cause of the limitation to near-unity indistinguishability for photons stemming from a TPE scheme is from the decay rates of $|X\rangle$ and $|XX\rangle$ and could be overcome by asymmetrical Purcell enhancement of the states in order to reduce spectral broadening of the biexciton and timing jitter of the exciton. This would as a result make the TPE scheme behave more like a TLS excited by a detuned laser and could be an ultimate scheme for realizing single-photon sources.

For the QD studied a large amount of power-dependent blinking has been observed when doing TPE, which is not present under RE. This does suggest the presence of a power-dependent dark state, which is not desirable. It should be investigated whether this is a condition connected to doing TPE or whether it is specific for the QD on the sample where this work has been conducted.

CHAPTER 8 Conclusion

This thesis has covered a range of topics surrounding the generation of quantum dot single photons. In particular with attention to how one quantify a good single-photon source and how to generate such high-quality photons in photonic crystal waveguides. Below, I summarize some of the main takeaways.

Quantum dots embedded in photonic crystal waveguides already show promising results as a single-photon source with high indistinguishability [11]. They work well because of the suppression of laser scattering and are promising platforms because of the possibility of integration in solid state systems.

High indistinguishability is achieved through resonant excitation by a pulsed laser as time jitter is suppressed, and it is therefore the scheme of choice for generating single photons (*Chapter 7*). This however comes with the challenge of suppressing laser scattering in the collected emission, which decreases purity.

The focus of this thesis has been on investigating how the wavefront and shape of the excitation pulse influences the purity of the collected emission.

For example, by choosing a polarization where the excitation laser is well coupled to the orientation of the dipole that is aligned with the waveguide, one efficiently excites the quantum dot (*Chapter 5*). However, the laser polarization should also still be aligned as to couple a small amount to the out-of-plane mode in order to not use to much power to reach π-pulse, which would introduce scattering.

It has also been reported how modifying the phase of the incident wavefront can be used to suppress laser scattering at any polarization (*Chapter 5*).

Furthermore, the importance of optimal pulse duration has been discussed. Pulse duration of the excitation laser τ_{laser} should not be too long (compared to the lifetime of the quantum dot τ_0) as this increases the probability for re-excitation. However, too short pulses increases the laser scattering in the system (*Chapter 6*). This work suggests that the preferred pulse width is around $\tau_{laser}/\tau_0 \sim 0.06$.

The best achieved measurements were of single photons with purity $g^2(0) = 0.0086 \pm 0.0013$ and an indistinguishability of $V = 96 \pm 1\%$. This was achieved with an efficiency of $\eta_{tot} = 6 \pm 1\%$. Achieving such a high-quality concurrently across all three parameters shows how quantum dots embedded in photonic crystal waveguides are promising candidates as state-of-the-art single-photon sources.

Outlook

The efficiency is currently limited by collection optics. However, this can readily be improved by employing on-chip fiber couplers, so the collection fiber is directly coupled to the nanostructures which avoids all optical losses [24]. This together with using a one-sided nanostructure would increase the efficiency to $16 \pm 1\%$.

The importance of generating single photons that simultaneously exhibit high purity, indistinguishably, and efficiency is clear when one considers the possible applications in

quantum information. The first step of protocols are often to realize high-quality single photons. And often more than one source is required. However, one source can be transformed into M single-photon sources by demultiplexing, where the source is fed through different spatial modes. This concept has previously been demonstrated utilizing a source with $g^2(0) = 0.05$ and $V > 90\%$. Where a four-photon detection rate of > 1 Hz was achieved [40]. This demonstrates an approach for scaling up quantum dot single-photon sources toward experiments that require multiple sources. And it would directly be improved by utilizing a higher quality source.

For further research it would be interesting to consider how further pulse shaping of the incident wavefront affects the emission. E.g. one could use a spatial light modulator (SLM) to study and optimize the wavefront by creating non-gaussian pulse shapes. One could also go a step further and use the SLM to simultaneously excite multiple quantum dots at different positions. This could be an approach for studying coupling between quantum dots.

It has also been shown how adjusting the phase of the wavefront improved purity while selectively exciting a given polarized dipole, this has direct consequences for spin-photon interface and multi-photon protocols [41].

As a natural next step for improving the single photon generation, I would suggest to implement all three aspects of pulse shaping that has here been investigated on the same quantum dot. That is, when one has found a quantum dot of interest then the impurity should be improved by optimizing 1) the excitation polarization, 2) the pulse duration, and 3) the phase of the wavefront.

Furthermore, the system performs very well, however a feedback system that monitors the impurity and corrects for any increase of scattered laser would readily improve the stability of the setup. Which would allow for longer integration time when performing hands-free measurements, resulting in lower purity estimates.

Bibliography

[1] P. Lodahl, S. Mahmoodian, and S. Stobbe, "Interfacing single photons and single quantum dots with photonic nanostructures," *Reviews of Modern Physics*, vol. 87, pp. 347–400, May 2015.

[2] J. Kołodyński, A. Máttar, P. Skrzypczyk, E. Woodhead, D. Cavalcanti, K. Banaszek, and A. Acín, "Device-independent quantum key distribution with single-photon sources," *Quantum*, vol. 4, p. 260, Apr. 2020.

[3] J. Borregaard, H. Pichler, T. Schröder, M. D. Lukin, P. Lodahl, and A. S. Sørensen, "One-way quantum repeater based on near-deterministic photon-emitter interfaces," *Physical Review X*, vol. 10, June 2020.

[4] A. Aspuru-Guzik and P. Walther, "Photonic quantum simulators," *Nature Physics*, vol. 8, pp. 285–291, Apr. 2012.

[5] G. J. Milburn and S. Basiri-Esfahani, "Quantum optics with one or two photons," *Proceedings of the Royal Society A: Mathematical, Physical and Engineering Sciences*, vol. 471, p. 20150208, Aug. 2015.

[6] D. A. Steck, *Quantum and Atom Optics*. available online at http://steck.us/teaching, 2006.

[7] R. Loudon, *The quantum theory of light*. Oxford New York: Oxford University Press, 2000.

[8] P. Lodahl, "Quantum-dot based photonic quantum networks," *Quantum Science and Technology*, vol. 3, p. 013001, oct 2017.

[9] P. Michler, ed., *Quantum Dots for Quantum Information Technologies*. Springer International Publishing, 2017.

[10] T. Pregnolato, X.-L. Chu, T. Schröder, R. Schott, A. D. Wieck, A. Ludwig, P. Lodahl, and N. Rotenberg, "Deterministic positioning of nanophotonic waveguides around single self-assembled quantum dots," *APL Photonics*, vol. 5, p. 086101, Aug. 2020.

[11] R. Uppu, F. T. Pedersen, Y. Wang, C. T. Olesen, C. Papon, X. Zhou, L. Midolo, S. Scholz, A. D. Wieck, A. Ludwig, and P. Lodahl, "Scalable integrated single-photon source," *ArXiv eprints*, vol. arXiv:2003.08919, 2020.

[12] A. Javadi, I. Söllner, M. Arcari, S. L. Hansen, L. Midolo, S. Mahmoodian, G. Kiršanskė, T. Pregnolato, E. H. Lee, J. D. Song, S. Stobbe, and P. Lodahl, "Single-photon non-linear optics with a quantum dot in a waveguide," *Nature Communications*, vol. 6, Oct. 2015.

[13] F. T. Pedersen, Y. Wang, C. T. Olesen, S. Scholz, A. D. Wieck, A. Ludwig, M. C. Löbl, R. J. Warburton, L. Midolo, R. Uppu, and P. Lodahl, "Near transform-limited quantum dot linewidths in a broadband photonic crystal waveguide," *ACS Photonics*, Aug. 2020.

[14] C. Santori, D. Fattal, J. Vučković, G. S. Solomon, and Y. Yamamoto, "Indistinguishable photons from a single-photon device," *Nature*, vol. 419, pp. 594–597, Oct. 2002.

[15] C. K. Hong, Z. Y. Ou, and L. Mandel, "Measurement of subpicosecond time intervals between two photons by interference," *Physical Review Letters*, vol. 59, pp. 2044–2046, Nov. 1987.

[16] L. Mandel, "Quantum effects in one-photon and two-photon interference," *Reviews of Modern Physics*, vol. 71, pp. S274–S282, Mar. 1999.

[17] A. M. Brańczyk, "Hong-ou-mandel interference," *ArXiv eprints*, vol. arXiv:1711.00080, Oct. 2017.

[18] C. C. Gerry, *Introductory quantum optics*. Cambridge, UK New York: Cambridge University Press, 2005.

[19] Z. Ou, C. Hong, and L. Mandel, "Relation between input and output states for a beam splitter," *Optics Communications*, vol. 63, pp. 118–122, July 1987.

[20] F. Liu, A. J. Brash, J. O'Hara, L. M. P. P. Martins, C. L. Phillips, R. J. Coles, B. Royall, E. Clarke, C. Bentham, N. Prtljaga, I. E. Itskevich, L. R. Wilson, M. S. Skolnick, and A. M. Fox, "High purcell factor generation of indistinguishable on-chip single photons," *Nature Nanotechnology*, vol. 13, pp. 835–840, July 2018.

[21] S. Kako, C. Santori, K. Hoshino, S. Götzinger, Y. Yamamoto, and Y. Arakawa, "A gallium nitride single-photon source operating at 200 k," *Nature Materials*, vol. 5, pp. 887–892, Oct. 2006.

[22] X. Zhou, I. Kulkova, T. Lund-Hansen, S. L. Hansen, P. Lodahl, and L. Midolo, "High-efficiency shallow-etched grating on GaAs membranes for quantum photonic applications," *Applied Physics Letters*, vol. 113, p. 251103, Dec. 2018.

[23] R. Uppu, H. T. Eriksen, H. Thyrrestrup, A. D. Uğurlu, Y. Wang, S. Scholz, A. D. Wieck, A. Ludwig, M. C. Löbl, R. J. Warburton, P. Lodahl, and L. Midolo, "On-chip deterministic operation of quantum dots in dual-mode waveguides for a plug-and-play single-photon source," *Nature Communications*, vol. 11, July 2020.

[24] A. D. Uğurlu, H. Thyrrestrup, R. Uppu, C. Ouellet-Plamondon, R. Schott, A. D. Wieck, A. Ludwig, P. Lodahl, and L. Midolo, "Suspended spot-size converters for scalable single-photon devices," *Advanced Quantum Technologies*, vol. 3, p. 1900076, Aug. 2019.

[25] T. Chaigne, O. Katz, A. C. Boccara, M. Fink, E. Bossy, and S. Gigan, "Controlling light in scattering media non-invasively using the photoacoustic transmission matrix," *Nature Photonics*, vol. 8, pp. 58–64, Nov. 2013.

[26] M. S. Kirilenko, P. A. Khorin, and A. P. Porfirev, "Wavefront analysis based on zernike polynomials," in *Proceedings of International conference Information Technology and Nanotechnology (ITNT-2016)*, Samara State Aerospace University, Image Processing Systems Institute, Russian Academy of Sciences, 2016.

[27] Wikipedia, "Zernike polynomials," 2020.

[28] A. Vyas, M. B. Roopashree, R. K. Banyal, and B. R. Prasad, "Spatial light modulator for wavefront correction," *ArXiv eprints*, vol. arXiv:0909.3413, May 2009.

[29] M. J. Kewming, S. Shrapnel, and G. J. Milburn, "Quantum enhanced agents," *ArXiv eprints*, vol. arXiv:2007.04426, 2020.

[30] K. A. Fischer, L. Hanschke, M. Kremser, J. J. Finley, K. Müller, and J. Vučković, "Pulsed rabi oscillations in quantum two-level systems: beyond the area theorem," *Quantum Science and Technology*, vol. 3, p. 014006, dec 2017.

[31] H. Ollivier, S. E. Thomas, S. C. Wein, I. M. de Buy Wenniger, N. Coste, J. C. Loredo, N. Somaschi, A. Harouri, A. Lemaitre, I. Sagnes, C. S. L. Lanco, C. Anton, O. Krebs, and P. Senellart, "Hong-ou-mandel interference with imperfect single photon sources," *ArXiv eprints*, vol. arXiv:2005.01743, May 2020.

[32] K. A. Fischer, K. Müller, K. G. Lagoudakis, and J. Vučković, "Dynamical modeling of pulsed two-photon interference," *New Journal of Physics*, vol. 18, p. 113053, Nov. 2016.

[33] A. Z. Genack and J. M. Drake, "Relationship between optical intensity, fluctuations and pulse propagation in random media," *Europhysics Letters (EPL)*, vol. 11, pp. 331–336, feb 1990.

[34] D. Huber, M. Reindl, Y. Huo, H. Huang, J. S. Wildmann, O. G. Schmidt, A. Rastelli, and R. Trotta, "Highly indistinguishable and strongly entangled photons from symmetric GaAs quantum dots," *Nature Communications*, vol. 8, May 2017.

[35] L. Schweickert, K. D. Jöns, K. D. Zeuner, S. F. C. da Silva, H. Huang, T. Lettner, M. Reindl, J. Zichi, R. Trotta, A. Rastelli, and V. Zwiller, "On-demand generation of background-free single photons from a solid-state source," *Applied Physics Letters*, vol. 112, p. 093106, Feb. 2018.

[36] L. Hanschke, K. A. Fischer, S. Appel, D. Lukin, J. Wierzbowski, S. Sun, R. Trivedi, J. Vučković, J. J. Finley, and K. Müller, "Quantum dot single-photon sources with ultra-low multi-photon probability," *npj Quantum Information*, vol. 4, Sept. 2018.

[37] R. Trivedi, K. A. Fischer, J. Vučković, and K. Müller, "Generation of non-classical light using semiconductor quantum dots," *Advanced Quantum Technologies*, vol. 3, p. 1900007, Jan. 2020.

[38] E. Schöll, L. Schweickert, L. Hanschke, K. D. Zeuner, F. Sbresny, T. Lettner, R. Trivedi, M. Reindl, S. F. C. da Silva, R. Trotta, J. J. Finley, J. Vučković, K. Müller, A. Rastelli, V. Zwiller, and K. D. Jöns, "The crux of using the cascaded emission of a 3–level quantum ladder system to generate indistinguishable photons," *ArXiv eprints*, vol. arXiv:2006.05476v2, 2020.

[39] F. D. Stefani, J. P. Hoogenboom, and E. Barkai, "Beyond quantum jumps: Blinking nanoscale light emitters," *Physics Today*, vol. 62, pp. 34–39, Feb. 2009.

[40] T. Hummel, C. Ouellet-Plamondon, E. Ugur, I. Kulkova, T. Lund-Hansen, M. A. Broome, R. Uppu, and P. Lodahl, "Efficient demultiplexed single-photon source with a quantum dot coupled to a nanophotonic waveguide," *Applied Physics Letters*, vol. 115, p. 021102, July 2019.

[41] D. Ding, M. H. Appel, A. Javadi, X. Zhou, M. C. Löbl, I. Söllner, R. Schott, C. Papon, T. Pregnolato, L. Midolo, A. D. Wieck, A. Ludwig, R. J. Warburton, T. Schröder, and P. Lodahl, "Coherent optical control of a quantum-dot spin-qubit in a waveguide-based spin-photon interface," *Physical Review Applied*, vol. 11, Mar. 2019.